



Bifunctional $\text{Bi}_{12}\text{O}_{17}\text{Cl}_2/\text{MIL-100}(\text{Fe})$ composites toward photocatalytic $\text{Cr}(\text{VI})$ sequestration and activation of persulfate for bisphenol A degradation

Chen Zhao^{a,b}, Jiasheng Wang^b, Xi Chen^b, Zhihua Wang^{a,*}, Haodong Ji^c, Long Chen^c, Wen Liu^c, Chong-Chen Wang^{b,d,**}

^a State Key Laboratory of Chemical Resource Engineering, Beijing University of Chemical Technology, Beijing 100029, China

^b Beijing Key Laboratory of Functional Materials for Building Structure and Environment Remediation, Beijing University of Civil Engineering and Architecture, Beijing 100044, China

^c College of Environmental Sciences and Engineering, Peking University, Key Laboratory of Water and Sediment Sciences, Ministry of Education, Beijing 100871, China

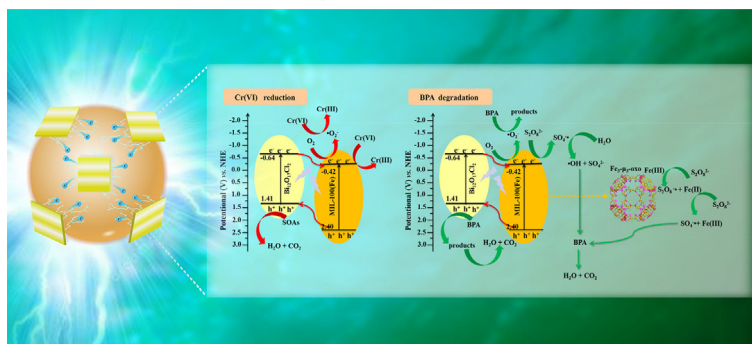
^d College of Environmental Science and Engineering, North China Electric Power University, Beijing 102206, China

HIGHLIGHTS

- $\text{Bi}_{12}\text{O}_{17}\text{Cl}_2/\text{MIL-100}(\text{Fe})$ (BMx) was constructed by facile ball-milling method.
- BM200 composite was an efficient photocatalyst for $\text{Cr}(\text{VI})$ and BPA cleanup.
- BM200/light/PS system exhibited synergistic effect in BPA degradation.
- BM200 showed good reusability and high stability.
- DFT calculation with high Fukui index interpreted the easy-attacking sites on BPA.

GRAPHICAL ABSTRACT

Bismuth-rich $\text{Bi}_{12}\text{O}_{17}\text{Cl}_2/\text{MIL-100}(\text{Fe})$ composites were firstly fabricated to achieve efficient $\text{Cr}(\text{VI})$ sequestration and BPA degradation with the addition of persulfate PS under white light illumination.



ARTICLE INFO

Article history:

Received 18 June 2020

Received in revised form 21 August 2020

Accepted 21 August 2020

Available online 22 August 2020

Editor: Dimitra A Lambropoulou

Keywords:

Metal-organic frameworks

$\text{Bi}_{12}\text{O}_{17}\text{Cl}_2$

$\text{Cr}(\text{VI})$

ABSTRACT

Bifunctional $\text{Bi}_{12}\text{O}_{17}\text{Cl}_2/\text{MIL-100}(\text{Fe})$ composite (BMx) was firstly constructed via facile ball-milling method. The optimal BM200 was highly efficient for $\text{Cr}(\text{VI})$ sequestration and activation of persulfate (PS) for bisphenol A (BPA) decomposition under white light illumination, which was much more remarkable than the pristine MIL-100(Fe) and $\text{Bi}_{12}\text{O}_{17}\text{Cl}_2$, respectively. Furthermore, the photocatalytic reduction efficiency can be significantly improved via the addition of some green small organic acids (SOAs). As well, the BPA degradation can be achieved over an extensive initial pH range of 3.0–11.0. When the PS concentration increased to more than 2.0 mM, the BPA degradation efficiency decreased due to the $\text{SO}_4^{\bullet-}$ self-scavenging effect. It was also found that the co-existence of inorganic anions like H_2PO_4^- , HCO_3^- , SO_4^{2-} , Cl^- and NO_3^- could decelerate the BPA degradation. The excellent photocatalytic $\text{Cr}(\text{VI})$ reduction and persulfate activation performances originated from both MIL-100(Fe) with excellent PS activation ability and $\text{Bi}_{12}\text{O}_{17}\text{Cl}_2$ with a favorable band position, which not only enabled the efficient separation of charges but also accelerated the formation of $\text{SO}_4^{\bullet-}$ radicals. The BM200 displayed

* Corresponding author.

** Correspondence to: C.-C. Wang, Beijing University of Civil Engineering and Architecture, Beijing 100044, China; North China Electric Power University, Beijing 102206, China.
E-mail addresses: zhwang@mail.buct.edu.cn (Z. Wang), chongchenwang@126.com, wangchongchen@bucea.edu.cn (C.-C. Wang).

1. Introduction

Nowadays, water environments are threatened by a large amount of reluctant contaminants, such as heavy metals (HMs) (Bolisetty et al., 2019) and endocrine disrupting chemicals (EDCs) (Leusch et al., 2019). Cr(VI) is one of the most malignant HMs due to its strong carcinogenic and mutagenic properties. The World Health Organization (WHO) has rigidly supervised that the content of Cr(VI) ions inside the human body should not exceed 0.05 mg/L (Cedeño et al., 2017). The common treatment method for Cr-containing wastewater is to reduce Cr(VI) to Cr(III), which is extremely weak in toxicity and can be easily removed via the post-processing methods, such as precipitation and adsorption treatments (Yang et al., 2014). Among a variety of Cr(VI) control technologies, relying on the photo-generated electrons by photocatalysts is very attractive because it offers the possibility of using sustainable solar energy to facilitate reactions under mild conditions (Wang et al., 2016).

Meanwhile, bisphenol A (BPA) is a typical EDCs with certain toxicity and teratogenicity, and its long-term exposure might induce ovarian cancer, prostate cancer, leukemia. Its predicted no effect concentration (PNEC) had been required to be less than 0.06 $\mu\text{g/L}$ in 2011 (Wright-Walters et al., 2011). Furthermore, the estimated half-life of BPA in various water environments is approximately 160 days (Zhao et al., 2018b), so traditional wastewater treatment techniques employing carbon adsorption or activated sludge are not capable to remove BPA efficiently. Advanced oxidation processes (AOPs) are capable of decomposing different kinds of organic pollutants in aquatic environments, even at trace levels (Yang et al., 2020). Sulfate free radical ($\text{SO}_4^{\bullet-}$) based treatment techniques, as one of the most high-efficiency AOPs, have been widely concerned about degradation of recalcitrant pollutants in water through activation of persulfate (PS) (Wang et al., 2019a). Being compared with the traditional hydroxyl radical ($\bullet\text{OH}$) based AOPs, its impressive advantages are deemed as powerful oxidizability (2.5–3.1 V vs. SHE) over a broad pH range (2.0–11.0) with a prolonged half-life (30–40 μs) (Wang et al., 2019a). Up to now, a mass of methods have been dedicated to active $\text{SO}_4^{\bullet-}$ production (Matzek and Carter, 2016). In particular, it needs to be emphasized that PS activation triggered by photocatalysis has received widespread attention due to its potential to produce $\text{SO}_4^{\bullet-}$ under mild conditions and the use of sustainable solar energy (Du et al., 2020; Gao et al., 2017; Gong et al., 2018; Tang et al., 2019).

Metal-organic frameworks (MOFs) can be deemed as a sort of heterogeneous catalysts with impressive photocatalytic activities (Wang et al., 2014). Prominent Fe-based MOFs represented by MILs-MOFs exhibit competitive capacity for absorbing visible light due to the existence of trimeric $\text{Fe}_3-\mu_3\text{-oxo}$ clusters (Zheng and Jiao, 2017). More importantly, because the existence of coordinatively unsaturated Fe sites in the abundant surface of Fe-containing MOFs, thus introducing oxidants like persulfate (PS) as electron acceptors is an advisable way to activation of reactive oxygen species (ROS). Furthermore, the addition of PS in reaction system is conducive to accelerate the separation and migration of photo-generated electron-hole pairs during photocatalytic process, which is extremely beneficial for improving the corresponding catalytic efficiency. For instance, Gao et al. (2017) reported that Acid Orange 7 can be efficiently photodegraded over MIL-53(Fe) under visible LED light irradiation with the assistance of PS. Lin et al. (2020) constructed a MIL-88(Fe)/PS/visible light reaction system for high-efficiency decomposition of BPA in simulated wastewater. However, it is a remarkable fact that the photocatalytic efficiency of single-component MOF is typically unsatisfied owing to their inferior

electronic conductance (Wang et al., 2020). To date, constructing heterojunction materials with Fe-containing MOFs and other highly conductive semiconductors is a popular strategy. Gong et al. (2018) fabricated g- $\text{C}_3\text{N}_4/\text{MIL-101(Fe)}$ composites through a facile hydrothermal method, which exhibited improved catalytic efficiency for BPA degradation in the presence of PS under visible light irradiation. Miao et al. (2019) synthesized $\text{BiOCl}/\text{MIL-53(Fe)}$ composite as an efficient visible-light-driven catalyst to activate PS for the degradation of Rhodamine B. The superior performances were attributed to the strong interfacial bonding between the two components and their appropriate band alignment, which not only accelerated the transfer rate of photo-generated charge carries, but also dramatically enhanced the PS activation efficiency. Nevertheless, to best our knowledge, there was no research about PS activation triggered by photocatalysis for contaminant removal over MIL-100(Fe) or its composites.

Recently, Bi-based semiconductors have gathered considerable interests by virtue of their superior availability, robust stability and non-toxicity (Wang et al., 2020). Among them, bismuth-rich bismuth oxyhalides ($\text{Bi}_x\text{O}_y\text{X}_z$, $\text{X} = \text{Cl}, \text{Br}$ and I) photocatalysts have been proved to possess more negative conduction band positions that meet most of the reaction potentials (Jin et al., 2017). $\text{Bi}_{12}\text{O}_{17}\text{Cl}_2$ is an emerging $\text{Bi}_x\text{O}_y\text{X}_z$ photocatalyst with the band gap of 2.07 eV, as well, its conduction band position is negative enough (approximately -0.56 eV) to accomplish Cr(VI) reduction and molecular O_2 activation (Wang et al., 2017a). Nevertheless, the photocatalytic activity of $\text{Bi}_{12}\text{O}_{17}\text{Cl}_2$ is not effective enough for actual applications due to its low quantum yield. Therefore, the preparation of $\text{Bi}_{12}\text{O}_{17}\text{Cl}_2$ -based composites has been explored, such as $\text{WO}_3/\text{Bi}_{12}\text{O}_{17}\text{Cl}_2$ (Zheng et al., 2018), $\text{PANI}/\text{Bi}_{12}\text{O}_{17}\text{Cl}_2$ (Xu et al., 2019), $\text{AgI}/\text{Bi}_{12}\text{O}_{17}\text{Cl}_2$ (Zhou et al., 2018), etc. The above composites showed enhanced photocatalytic degradation performance than pristine $\text{Bi}_{12}\text{O}_{17}\text{Cl}_2$, however, the study on $\text{Bi}_{12}\text{O}_{17}\text{Cl}_2$ -based composites for bifunctional Cr(VI) reduction and organic pollutants degradation has not been reported so far. Consequently, it is imperative to fabricate a novel class of photocatalysts by constructing a material with its own respective functions and matching the energy levels of $\text{Bi}_{12}\text{O}_{17}\text{Cl}_2$.

In order to make full use of the advantages of MIL-100(Fe) and $\text{Bi}_{12}\text{O}_{17}\text{Cl}_2$, the $\text{Bi}_{12}\text{O}_{17}\text{Cl}_2/\text{MIL-100(Fe)}$ (BMx) composites were firstly constructed via adopting ball-milling method. As a result, the as-prepared composites displayed remarkably enhanced photocatalytic activities toward the Cr(VI) reduction and BPA degradation with addition of PS under white light irradiation. Furthermore, the reaction mechanisms were also confirmed by multi-class of characterization techniques, such as radicals trapping experiments, photoelectric chemical analysis and ESR testing. The BPA degradation pathway was ascertained based on UHPLC-MS analysis and density functional theory (DFT) calculation.

2. Experimental

2.1. Preparation of photocatalysts

All chemicals and solvents were of analytical-grade and employed without further purification. The $\text{Bi}_{12}\text{O}_{17}\text{Cl}_2$ nanobelts were synthesized via the solvothermal method, which is identical to the reported research (Wang et al., 2017a). Meanwhile, the MIL-100(Fe) nanospheres were prepared as reported previously with a few modifications (Xu et al., 2017). Briefly, 54.04 mg $\text{FeCl}_3 \cdot 6\text{H}_2\text{O}$ and 28.16 mg trimesic acid (1,3,5-BTC) were dissolved in 5.0 mL glycol and 5.0 mL *N,N*-Dimethylformamide (DMF), respectively. Afterwards, the resulting suspension was transferred into an autoclave with Teflon linear (25 mL)

and kept at 120 °C for 12 h. Then, the autoclave must be cooled to room temperature, the pale red powders were obtained via centrifugation and washing cycles. The collected materials were finally re-heated at 60 °C for 6 h for the subsequent analysis.

The $\text{Bi}_{12}\text{O}_{17}\text{Cl}_2/\text{MIL-100(Fe)}$ composites (BM_x , x is the mass of MIL-100(Fe) when the total weight of $\text{Bi}_{12}\text{O}_{17}\text{Cl}_2$ is 200 mg, such as BM_{100} , BM_{200} , BM_{300} , BM_{400} and BM_{500}) were fabricated by a planetary milling instrument operating for 20 min at a 30 Hz frequency (as illustrated in Scheme 1). The milling mediums were stainless steel balls with 10 mm or 20 mm in diameter. The details of the characterization methods (such as PXRD, FTIR, SEM, TEM, HRTEM, XPS, UV-vis DRS and ESR), photoelectrochemical measurements, degradation products' identification and DFT calculation were presented in Electronic Supplementary Information.

2.2. Catalytic efficiency evaluation

The photocatalytic efficiencies of the BM_x composites were explored under white light irradiation (300 W xenon lamp without use of cut-off filter, its wavelength distribution was depicted in Fig. S1). For the treatment of Cr(VI), 0.1 g of the as-prepared photocatalysts were added to a 200 mL Cr(VI) solution (10.0 mg/L) in a quartz reactor, and the initial pH values of the reaction system were regulated by adding 0.01 or 0.1 M NaOH and H_2SO_4 solution. After that, the mixture was constantly stirred for 1 h on a magnetic stirrer in dark condition to achieve the adsorption-desorption equilibrium. At pre-set period time, 2 mL suspensions were taken out and filtered via a 0.45 μm membrane for subsequent measurements. The content of Cr(VI) ions was tested by diphenylcarbazide (DPC) method using Bran+Luebb 3-AA3 AutoAnalyzer. For the BPA degradation, 0.05 g of the catalysts were dispersed into 200 mL of BPA aqueous solution (10.0 mg/L, pH = 5.2). After the establishment of adsorption-desorption equilibrium, 0.2 mM of $\text{Na}_2\text{S}_2\text{O}_8$ were added to the reactor. The content of BPA was measured by Vanquish Duo high performance liquid chromatograph (HPLC) equipped with a C18 column (2.1 mm \times 250 mm, 5.0 μm). The detection wavelength of the UV detector was set as 227 nm. Mobile phase was acetonitrile and water (55:45, v/v) and the flow rate was 0.2 mL/min. As to the cycling experiments, the BM_x composites were reused after each cycle of photoreduction or degradation experiment. The as-prepared catalysts were collected by filtration, followed by cleaning with ultrapure water and ethanol several times, respectively. Then, the obtained powders were dried overnight at room temperature. The used catalysts will inevitably be lost in each cycling experiment. Therefore, some fresh BM_x

composites were added to the reaction system to keep the amount of catalysts unchanged.

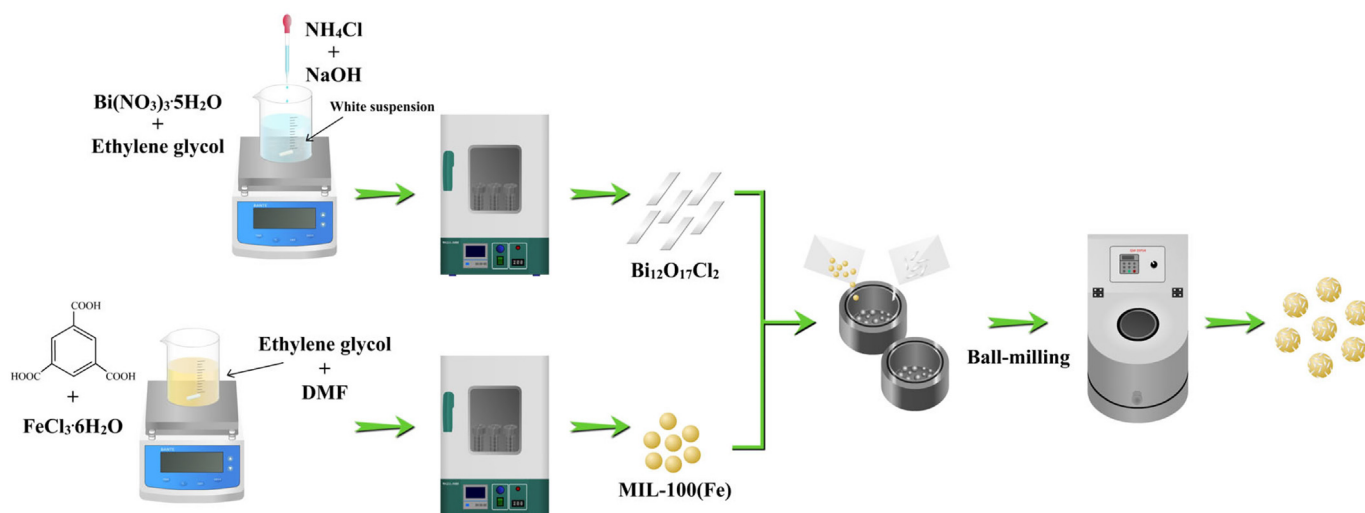
3. Results and discussion

3.1. Characterization

The powder X-ray diffraction (PXRD) spectra of $\text{Bi}_{12}\text{O}_{17}\text{Cl}_2$, MIL-100(Fe) and BM_x composites were shown in Fig. 1(a). The significant peaks of $\text{Bi}_{12}\text{O}_{17}\text{Cl}_2$, such as (113), (115), (117), (0012), (119), (220), (307) and (317) matched well with pure $\text{Bi}_{12}\text{O}_{17}\text{Cl}_2$ phase (JCPDS NO. 37-0702) (Chang et al., 2018). Meanwhile, the diffraction peaks of MIL-100(Fe) were in accordance with the simulated spectrum obtained from the single-crystal XRD data as well as previously reported MIL-100(Fe) (Xu et al., 2017). Obviously, the major diffraction peaks of BM_x composites accorded well with pristine $\text{Bi}_{12}\text{O}_{17}\text{Cl}_2$ and MIL-100(Fe), respectively. Moreover, it was observed that the diffraction peaks belonged to MIL-100(Fe) changed into stronger with its dosages continuously increased, revealing that the successful fabrication of BM_x composites. Additionally, no other impurity peaks were detected, meaning that the $\text{Bi}_{12}\text{O}_{17}\text{Cl}_2$ and MIL-100(Fe) maintained their crystalline structures during the ball-milling procedure.

Fig. 1(b) demonstrated the Fourier transform infrared (FTIR) spectra of the pure $\text{Bi}_{12}\text{O}_{17}\text{Cl}_2$, MIL-100(Fe) and BM_x composites. The strong characteristic peak at 3410 cm^{-1} was identified as the O—H vibration originating from bound or free water molecules (Tanwar et al., 2017). For all of the BM_x composites, the characteristic peaks at 469 cm^{-1} corresponded to the Bi—O functional groups (Di et al., 2015; Ding et al., 2017; Karthikeyan et al., 2014). The noticeable peaks at 711 and 812 cm^{-1} can be indexed to the 1,3,5-tri substitution of the benzene ring (Song et al., 2014). The characteristic peaks near 1709 cm^{-1} were ascribed to the stretching vibration of C=O bonds in 1,3,5-BTC. The strong peaks at 1384, 1450, 1575 and 1620 cm^{-1} should be indexed to the asymmetric/symmetric vibrations of carboxyl groups (Song et al., 2014). Therefore, the XRD and FTIR analysis jointly confirmed that the as-prepared BM_x composites contained $\text{Bi}_{12}\text{O}_{17}\text{Cl}_2$ and MIL-100(Fe) materials with various mass ratio.

In order to investigate the morphologies of the as-prepared materials, MIL-100(Fe), $\text{Bi}_{12}\text{O}_{17}\text{Cl}_2$ and BM_{200} were selected as the representative samples for the scanning electron microscope (SEM), transmission electron microscope (TEM) and high-resolution TEM observations (Fig. 2). From Fig. 2(a) and (d), MIL-100(Fe) showed the spherical shape with approximately 85–200 nm in diameter, which



Scheme 1. The fabrication procedure of the BM_x composites.

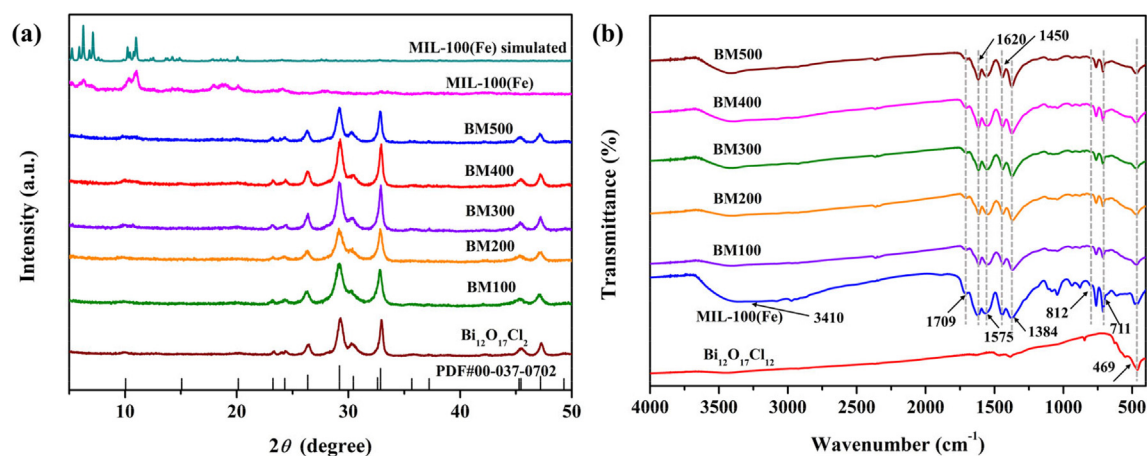


Fig. 1. PXRD and FTIR spectra of the $\text{Bi}_{12}\text{O}_{17}\text{Cl}_2$, MIL-100(Fe) and BMx composites.

was similar to the observation of MIL-100(Fe) reported previously (Xu et al., 2017). From Fig. 2(b) and (e), the pure $\text{Bi}_{12}\text{O}_{17}\text{Cl}_2$ nanosheets possessed an uneven size of 50–100 nm in width and 400–600 nm in length, which was also similar to the former studies (Chang et al., 2018; Wang et al., 2017a). Furthermore, the SEM and TEM micrographs

of BM200 (Fig. 2(c) and (f)) revealed that $\text{Bi}_{12}\text{O}_{17}\text{Cl}_2$ with different shapes were covered on the MIL-100(Fe) surface. The BM200 basically maintained the spherical morphology but the corresponding radius was extended to 200–400 nm. The HRTEM micrographs of BM200 (Fig. 2(g)–(i)) showed that the fringe spacings of 0.297, 0.246, 0.335,

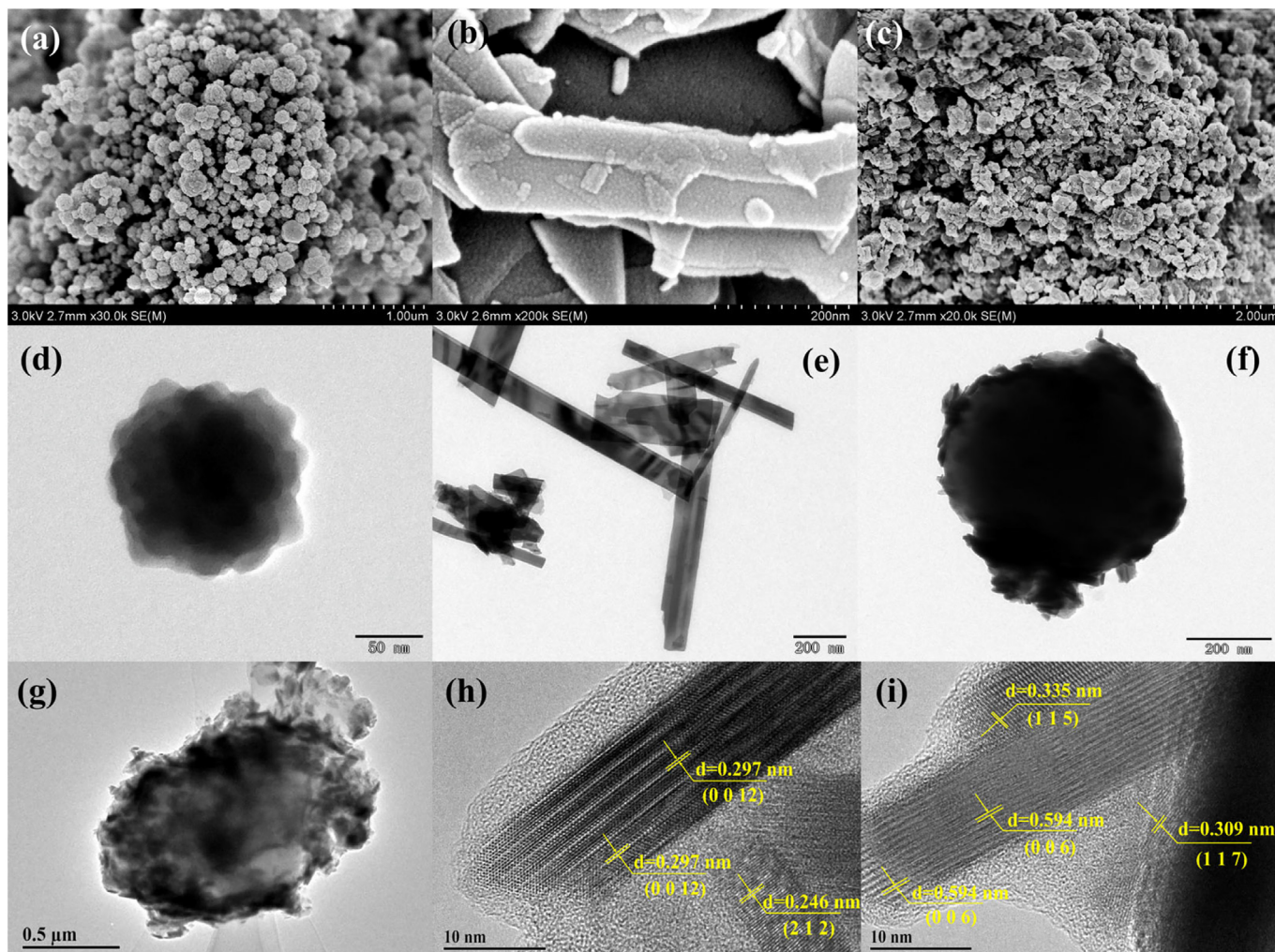


Fig. 2. SEM and TEM micrographs of (a, d) MIL-100(Fe), (b, e) $\text{Bi}_{12}\text{O}_{17}\text{Cl}_2$, (c, f) BM200 and (g–i) HRTEM micrographs of BM200.

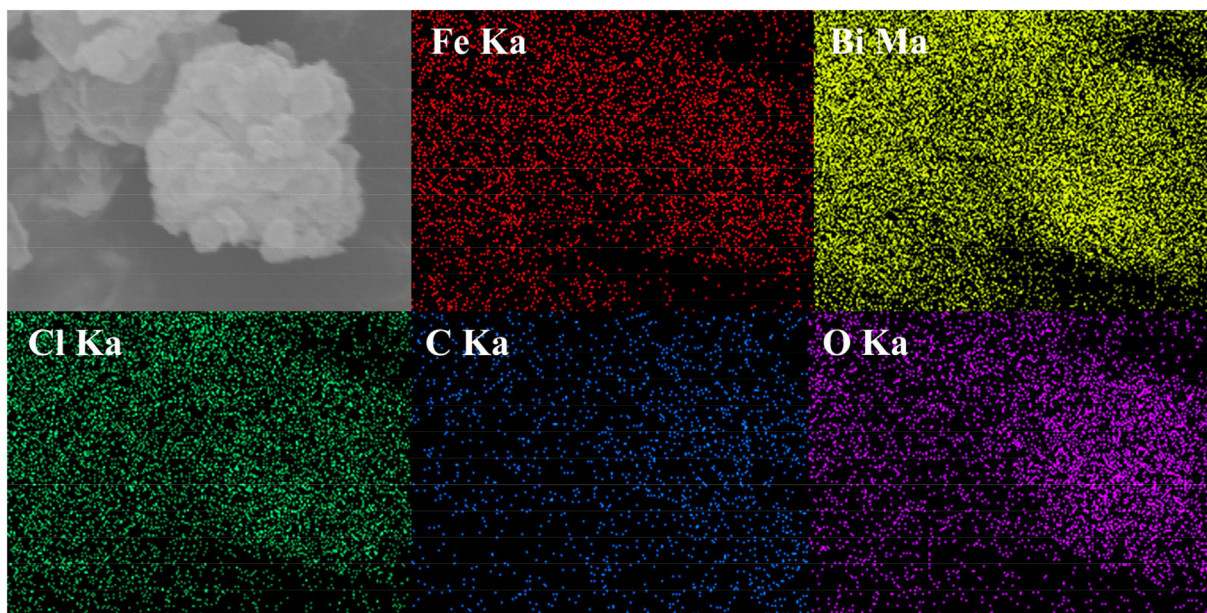


Fig. 3. EDS mapping micrographs of the as-prepared BM200.

0.309 and 0.594 nm could be assigned to the (0 0 12), (2 1 2), (1 1 5), (1 1 7) and (0 0 6) crystalline planes of $\text{Bi}_{12}\text{O}_{17}\text{Cl}_2$. And series of concentric rings in the selected area electron diffractograms (SAED) were shown in Fig. S2. The corresponding spot-rings can be indexed to the (2 0 14), (3 1 5), (2 1 10) and (3 1 9) crystalline planes of $\text{Bi}_{12}\text{O}_{17}\text{Cl}_2$ (PDF#00-037-0702). The HRTEM and SAED patterns indicated that $\text{Bi}_{12}\text{O}_{17}\text{Cl}_2$ was successfully incorporated into MIL-100(Fe) spherical structure. Additionally, as illustrated in Fig. 3, EDS-mapping was applied to detect the elements distribution of the BM200. It could be found that there were Fe, Bi, Cl, C, O elements in the BM200. And the results revealed that the above elements were uniformly distributed on the BM200 surface.

As shown in Fig. 4, the BM200 was selected as the representative of BMx composites to explore the binding states by X-ray photoelectron spectroscopy (XPS). In the survey spectrum (Fig. 4(a)), the C, O, Fe, Bi and Cl elements were detected, which was in line with the EDS result. The C 1s spectrum in Fig. 4(b) showed two main binding energy peaks at 284.9 and 288.9 eV, which should be attributed to benzoic rings and C=O bonds originated from 1,3,5-BTC (Xu et al., 2017). As for the O 1s spectrum (Fig. 4(c)), the two binding energies at 529.9 and 531.2 eV corresponded to the Bi—O and Fe—O structures of the BM200, respectively (Zhang et al., 2015a; Zhao et al., 2014). Fig. 4(d) illustrated the Fe 2p spectrum, the peaks at 712.5 and 725.4 eV can be attributed to the

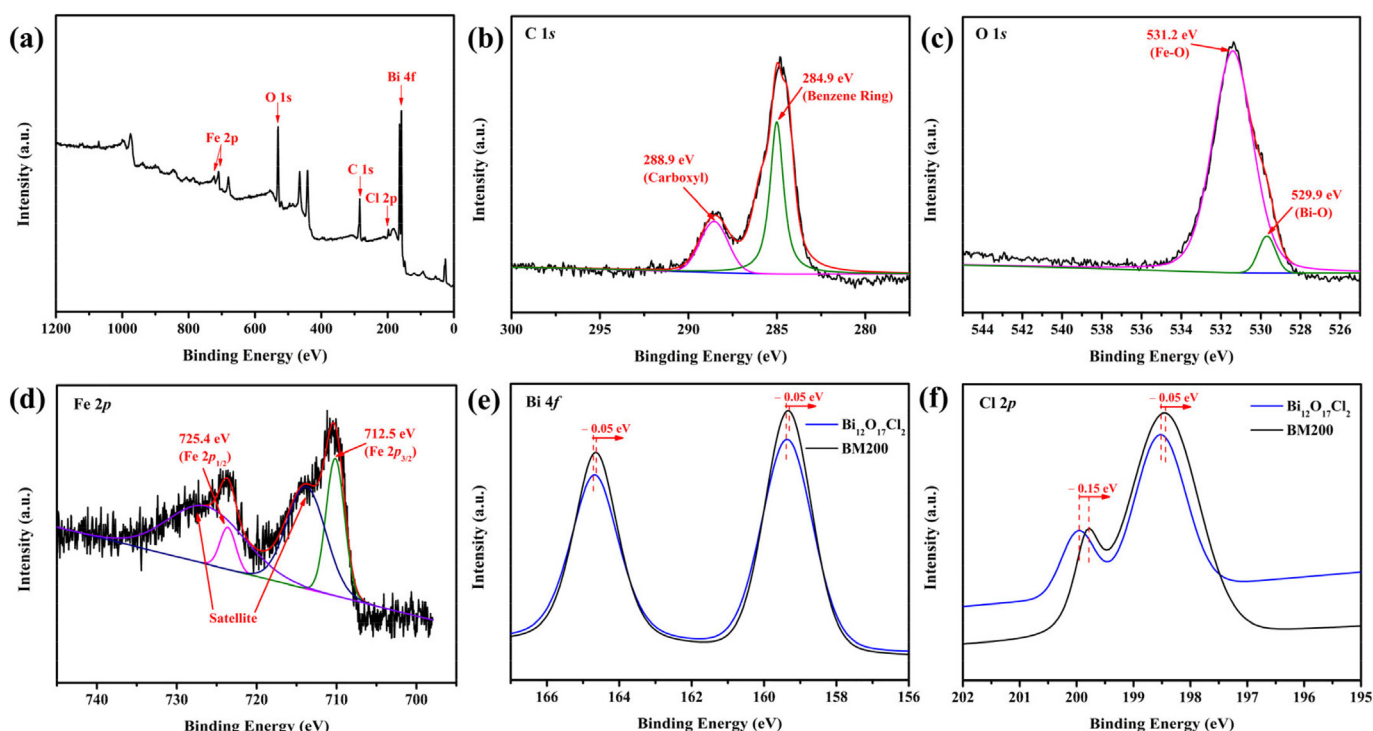


Fig. 4. High-resolution XPS of BM200: (a) survey, (b) C 1s, (c) O 1s, (d) Fe 2p; the comparisons of (e) Bi 4f and (f) Cl 2p spectra.

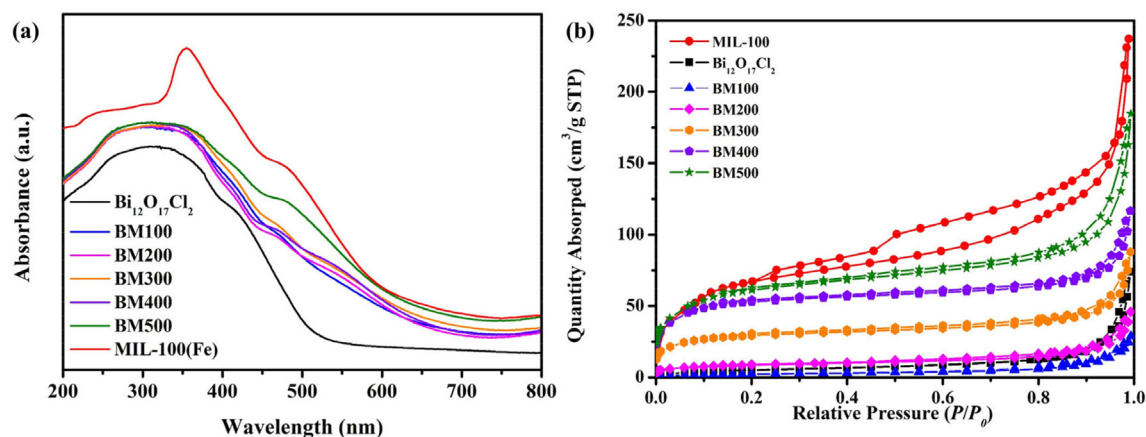


Fig. 5. (a) UV-vis DRS and (b) N_2 adsorption-desorption isotherms of the $Bi_{12}O_{17}Cl_2$, MIL-100(Fe) and BMx composites.

transitions of $Fe\ 2p_{3/2}$ and $Fe\ 2p_{1/2}$, respectively (Shen et al., 2014). Moreover, the two satellite peaks at 717.7 and 731.6 eV suggested that Fe(III) ions might exist in the BM200 structure (Zhang et al., 2015b). The XPS spectra of $Bi_{12}O_{17}Cl_2$ and BM200 in the region of Bi 4f and Cl 2p were illustrated in Fig. 4(e) and (f), respectively. For the BM200, the characteristic peaks at 159.3 and 164.6 eV in the Bi 4f spectrum were relevant to $Bi^{3+}\ 4f_{7/2}$ and $Bi^{3+}\ 4f_{5/2}$ (He et al., 2015). Similarly, the Cl 2p spectrum of the BM200 exhibited a couple of peaks at 199.8 and 199.2 eV, which was indexed to Cl $2p_{1/2}$ and Cl $2p_{3/2}$, respectively (He et al., 2015). Nevertheless, for the BM200, the energy shifts can be observed compared to the pure $Bi_{12}O_{17}Cl_2$, which should be described as the strong bonding interaction at MIL-100(Fe)/ $Bi_{12}O_{17}Cl_2$ interfaces.

Ultraviolet-visible diffuse reflectance spectra (UV-vis DRS) of the $Bi_{12}O_{17}Cl_2$, MIL-100(Fe) and BMx materials were depicted in Fig. 5(a). It can be found that the absorption edges of BMx materials were closely related to the pure $Bi_{12}O_{17}Cl_2$, indicating that all the as-prepared materials had the ability to absorb UV or visible light. Furthermore, MIL-100(Fe) had more powerful absorption capacity in both the UV and visible region than that of $Bi_{12}O_{17}Cl_2$, hence the absorbance of the BMx composites gradually increased with increasing MIL-100(Fe) content. This result further proved that the changes in optical band gaps were attributed to the intrinsic transition of the constituent photocatalysts. Additionally, the band gap energies (E_g) of the as-prepared materials were obtained using the Eq. (1):

$$\alpha(h\nu) = A(h\nu - E_g)^{n/2} \quad (1)$$

where, α , ν , and A are the absorption coefficient, light frequency and a constant, respectively. In this study, n was 4 for the indirect transition of $Bi_{12}O_{17}Cl_2$ (Wang et al., 2017a), whereas was 1 for the direct transition of MIL-100(Fe) (Du et al., 2019). Therefore, the E_g values of $Bi_{12}O_{17}Cl_2$ and MIL-100(Fe) were calculated to be 2.05 and 2.82 eV (Fig. S3(a)-(b)), respectively. The E_g values were 2.15, 2.28, 2.39, 2.57 and 2.68 eV for BM100, BM200, BM300, BM400 and BM500, respectively.

The Brunauer-Emmett-Teller (BET) surface area and porous structure of the as-prepared materials were explored by the N_2 adsorption-desorption measurement. As illustrated in Fig. 5(b), the isotherms of $Bi_{12}O_{17}Cl_2$, MIL-100(Fe) and BMx composites were recognized as type IV from the Brunauer-Deming-Deming-Teller (BDDT) classification, suggesting the existence of mesoporous structures (Yu and Ran, 2011). Furthermore, the BET surface areas of all the BMx composites were less than pristine MIL-100(Fe) (365.56 m^2/g) and greater than pristine $Bi_{12}O_{17}Cl_2$ (18.85 m^2/g) (Table 1). The most plausible reason was that a certain amount of the MOF porous channels was occupied

by the $Bi_{12}O_{17}Cl_2$ nanosheets. Meanwhile, the pore size (Fig. S4) and pore volumes (Table 1) of different materials showed the same trend as the BET surface area.

3.2. Catalytic properties of BMx composites

3.2.1. Cr(VI) reduction

Fig. 6(a) exhibited the photoreduction efficiencies of Cr(VI) over MIL-100(Fe), $Bi_{12}O_{17}Cl_2$ and BMx composites. After 120 min of photocatalytic process, only 51.1% and 61.4% of Cr(VI) can be removed by MIL-100(Fe) and $Bi_{12}O_{17}Cl_2$, respectively. As comparison, 47.4% of Cr(VI) was removed by $Bi_{12}O_{17}Cl_2$ and MIL-100(Fe) mixture in reaction solution. Obviously, the photocatalytic capacities of BMx composites were more superior than those of pristine $Bi_{12}O_{17}Cl_2$ and MIL-100(Fe), which can be ascribed to the improved light harvesting, increased active sites and accelerated charge carrier transfer in the BMx composites. Moreover, the BM200 displayed the highest activity, achieving 99.3% reduction efficiency within 120 min, which had 48.2% and 37.9% improvement compared to pristine MIL-100(Fe) and $Bi_{12}O_{17}Cl_2$, respectively. However, as shown in Fig. 6(a), the photoreduction efficiency slightly decreased with the increasing proportion of MIL-100(Fe) in the corresponding composite, such as BM300, BM400 and BM500. This phenomenon was mainly assigned to the excessive amount of MIL-100(Fe) might hinder the charges transfer at the interface of $Bi_{12}O_{17}Cl_2$ and MIL-100(Fe) heterojunction structure, which will be verified by the subsequent PL and electrochemical measurements. The pseudo-first-order kinetic (k) model (Eq. (2)) was applied to probe into the photocatalytic reaction kinetics quantitatively.

$$-\ln(C/C_0) = kt \quad (2)$$

under the identical reaction conditions, the k values of Cr(VI) reduction over the BM200 was $0.04082 \pm 0.003161\ min^{-1}$, which was 9.2 and 5.3 times higher than pristine MIL-100(Fe) ($0.00483 \pm 0.000205\ min^{-1}$) and $Bi_{12}O_{17}Cl_2$ ($0.00832 \pm 0.000262\ min^{-1}$), respectively (Fig. 6(b)).

Table 1
BET surface areas and pore volumes of various photocatalysts.

Material	BET surface area (m^2/g)	Pore volume (cm^3/g)
$Bi_{12}O_{17}Cl_2$	18.85	0.042
MIL-100(Fe)	365.56	0.257
BM100	8.85	0.021
BM200	29.87	0.037
BM300	98.73	0.079
BM400	177.08	0.119
BM500	210.42	0.172

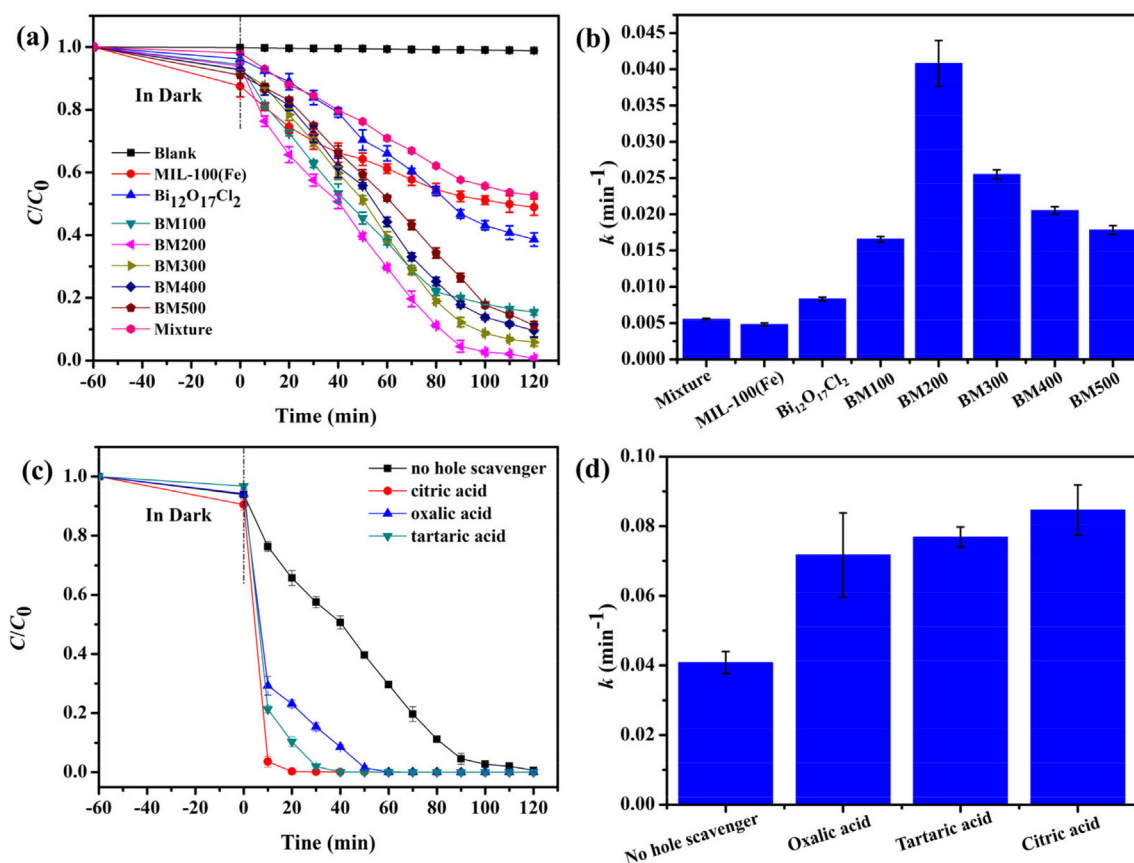


Fig. 6. (a) Photocatalytic performance toward Cr(VI) reduction over different photocatalysts under white light, (b) the corresponding k values over different photocatalysts, (c) photocatalytic reduction curves and (d) the k values with the presence of various SOAs. Condition: photocatalyst dosage = 0.5 g/L, Cr(VI) = 10.0 mg/L, pH = 2.0.

Therefore, BM200 was selected as the representative catalyst for the follow-up experimental analysis.

In order to further improve the photocatalytic Cr(VI) reduction rate, some small organic acids (SOAs, citric acid, oxalic acid and tartaric acid) were added in the reaction system (Fig. 6(c)). The results suggested that the presence of the above SOAs dramatically improved the photocatalytic efficiency of Cr(VI) reduction, nearly 100.0% Cr(VI) ions were removed within 20, 30, 50 min when the addition of citric acid, tartaric acid and oxalic acid, respectively. Furthermore, the apparent reaction rates reached to 0.07175 ± 0.012070 , 0.07684 ± 0.002934 and $0.08463 \pm 0.007227 \text{ min}^{-1}$ for oxalic acid, tartaric acid and citric acid, respectively (Fig. 6(d)). This result can be attributed to the SOAs were inclined to be absorbed on the surface of the photocatalysts, leading to be efficiently decomposed by the photo-generated holes, thereby significantly enhancing the separation efficiency of photo-generated charge carriers (Zhao et al., 2020). Furthermore, the photoreduction of Cr(VI) might proceed a charge-transfer-complex (CTC) mediated process, in which the charges were beneficial to migrate from SOAs to the conduction band of the BM200, resulting in strengthening the photocatalytic activity of Cr(VI) reduction. Meanwhile, some organic radicals generated in this process also made a contribution to the Cr(VI) photoreduction (Wang et al., 2010). Considering that the above SOAs were non-toxic and easy to be mineralized, hence the Cr(VI) reduction efficiencies with the presence of these green sacrificial agents were relatively competitive. It is generally believed that the photoreduction efficiency of Cr(VI) is greatly affected by the initial pH values. Therefore, to fully understand the effect of pH values on the Cr(VI) removal over the BM200, a series of investigations under various initial pH were done in this study. As illustrated in Fig. S5, the BM200 exhibited impressive photocatalytic performance under low-pH conditions owing to the presence of abundant H^+ (Wang et al., 2016). This result was consistent with

our previous reports on Cr(VI) photoreduction over MOFs-based photocatalysts (Chen et al., 2020; Yi et al., 2019; Zhao et al., 2020).

3.2.2. BPA degradation

The catalytic activities in BPA decomposition over $\text{Bi}_{12}\text{O}_{17}\text{Cl}_2$, MIL-100(Fe) and BMx materials were explored under white light illumination, while the control experiments were also implemented to compare the degradation efficiencies by different reactions with the same BPA initial concentration. As displayed in Fig. 7(a), the direct photolysis of BPA was non-significant in the absence of photocatalyst and PS under white light illumination (only 5.8%), suggesting that the BPA exhibited great stability. Meanwhile, the degradation activity of BPA by various photocatalysts were ineffective during illumination in the absence of PS, only $\text{Bi}_{12}\text{O}_{17}\text{Cl}_2$ exhibited higher capacity in decomposing BPA (nearly 57.4%), which was attributed to its negative position of conduction band (approximately -0.91 eV to -0.56 eV) might be inclined to generate large amounts of $\cdot\text{O}_2^-$ during the photocatalysis process, then the produced $\cdot\text{O}_2^-$ can be changed into $\cdot\text{OH}$ via multi-step free radical reaction processes (Eqs. (3)–(4)) (Wang et al., 2017a; Zhou et al., 2018). Moreover, previous studies had proved that the PS degradation could be activated by photolysis at wavelengths from 248 to 351 nm (Herrmann, 2007; Ismail et al., 2017). Considering that the spectral range of white light used in this study was about 340–660 nm (Fig. S1), so the BPA removal efficiency also reached 31.6% in light/PS system without the addition of any catalysts. More significantly, the addition of PS can prominently enhance the catalytic efficiency of BM200/light/PS system and 100.0% of BPA can be decomposed after 60 min illumination. This phenomenon suggested that BM200 combined with PS displayed a synergistic effect on BPA degradation under white light illumination (Eqs. (5)–(6)). Moreover, Fig. 7(b) exhibited the corresponding k values obtained by different reaction systems. The results revealed

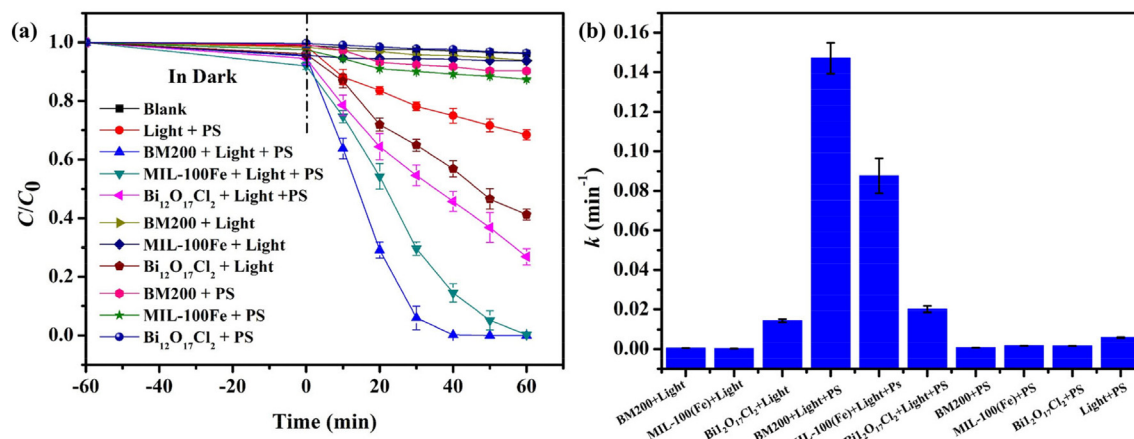


Fig. 7. (a) The photocatalytic activation of PS toward BPA degradation under white light, (b) the k values over different photocatalysts. Condition: photocatalyst dosage = 0.25 g/L, BPA = 10.0 mg/L, pH = 5.2, PS = 0.2 mM.

that the BM200/light/PS system was the optimal ($0.14713 \pm 0.007821 \text{ min}^{-1}$), which were 1.68, 7.29, 10.25, 263.04 and 201.78 times higher than those in MIL-100(Fe)/light/PS ($0.08762 \pm 0.008850 \text{ min}^{-1}$), $Bi_{12}O_{17}Cl_2$ /light/PS ($0.02018 \pm 0.001580 \text{ min}^{-1}$), $Bi_{12}O_{17}Cl_2$ /light ($0.01435 \pm 0.000764 \text{ min}^{-1}$), BM200/light ($0.00056 \pm 0.000006 \text{ min}^{-1}$) and BM200/PS ($0.00073 \pm 0.000032 \text{ min}^{-1}$) systems, also revealing that both the PS and white light acted a crucial role in the BM200/light/PS system. Meanwhile, the mineralization of BPA by BM200/light/PS system was also evaluated by testing the TOC content of the reaction solutions. As shown in Fig. S6, a sharp increase in TOC concentration after the adsorption-desorption equilibrium process, which was ascribed to the dissolving-out behavior of the organic ligand from MIL-100(Fe). However, it can be found that 29.5% of TOC was removed after 60 min reaction. Considering that the aliphatic intermediates after ring-opening reactions were relatively stable, the complete mineralization of BPA could be achieved if the reaction time was sufficiently prolonged.



To elucidate the generated active radicals in the different reaction systems, ESR technique was carried out to demonstrate the synergistic effect between BM200 and PS under white light irradiation (Fig. 8). As illustrated in Fig. 8(a), the DMPO- $\bullet OH$ adducts with the characteristic intensities of 1:2:2:1 along with DMPO- $SO_4^{\bullet-}$ adducts were precisely detected for the BM200/light/PS, $Bi_{12}O_{17}Cl_2$ /light/PS, MIL-100(Fe)/light/PS systems, implying the production of $\bullet OH$ and $SO_4^{\bullet-}$ radicals in the above systems. As expected, the construction of composite between $Bi_{12}O_{17}Cl_2$ and MIL-100(Fe) might be beneficial to photo-generated electrons transfer, thereby facilitating the activation of PS and produce more prominent $\bullet OH$ signals. Furthermore, it was worth noting that the $\bullet OH$ signals for the BM200/light/PS system were much stronger than that of BM200/PS, revealing that the white light irradiation gave rise to produce much more $\bullet OH$ radicals. The produced $\bullet OH$ radicals might be derived from the interactions between $SO_4^{\bullet-}$ and H_2O/OH^- (Eqs. (7)–(8)) (Gong et al., 2018; Lin et al., 2020). Additionally, MIL-100(Fe)/PS and BM200/PS systems also showed the PS activation ability in the dark conditions (Fig. 8(a)), and the formed $SO_4^{\bullet-}$ signals might originate from the catalytic PS by $Fe_3-\mu_3$ -oxo clusters in MIL-100(Fe) via Eqs. (9)–(10). Meanwhile, the addition of PS can also excite the other O-containing active radicals. As illustrated in Fig. 8(b), the ESR signals of DMPO- $\bullet O_2^-$ adducts were also observed in the ESR spectra of BM200/light/PS, $Bi_{12}O_{17}Cl_2$ /light/PS and MIL-100(Fe)/light/PS systems, which were relatively stronger than that of BM200/light, $Bi_{12}O_{17}Cl_2$ /light and MIL-100(Fe)/light systems, indicating that the activation of PS might lead to

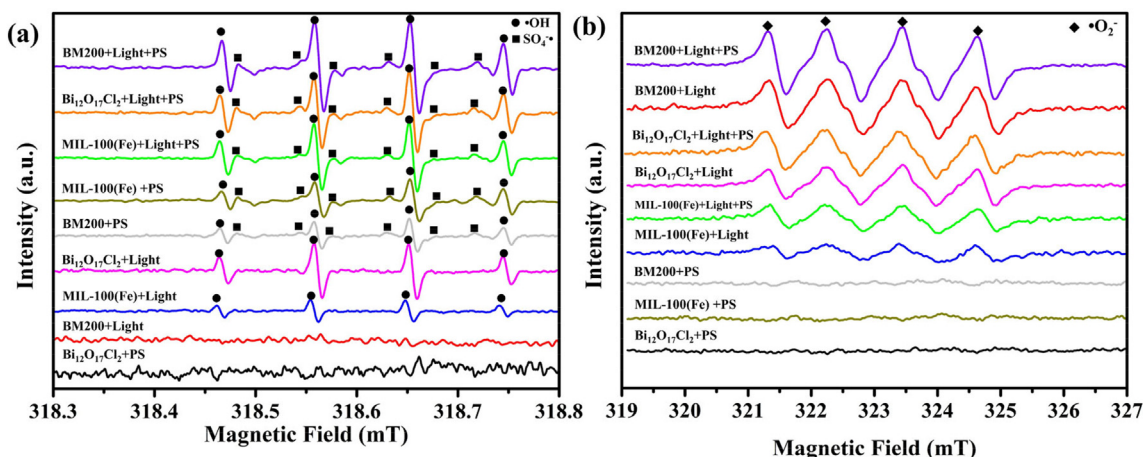
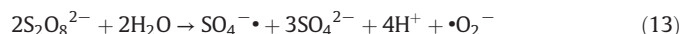
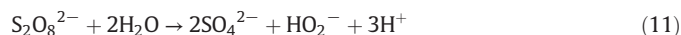
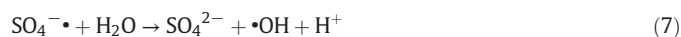


Fig. 8. ESR spectra detected in different reaction systems for (a) DMPO- $\bullet OH$ and (b) DMPO- $\bullet O_2^-$.

the enhanced $\bullet\text{O}_2^-$ production (Eqs. (11)–(13)), thereby improving the corresponding photocatalytic performance (Wang et al., 2019b).



3.2.2.1. Effect of initial pH on BPA degradation. The influence of initial pH values on the BPA degradation was explored, series-experiment of the pH values from 3.0 to 11.0 were performed. The results revealed that the decomposition of BPA in the BM200/light/PS system worked effectively over the wide pH range, the whole of degradation efficiencies reached above 99.4% after 60 min of white light irradiation (Fig. 9(a)). However, it was a remarkable fact that the removal rate of BPA decreased when the solution pH increased from 3.0 to 11.0. Moreover, it was worth noting that approximately 27.8% and 15.3% of BPA were removed within 60 min in the dark condition at pH = 3.0 and 11.0, respectively, which were much more efficient than that of other pH values. These phenomena should be ascribed to the zero potential of BM200 was estimated to be 4.09, suggesting that a positively charged surface of BM200 dispersion in aqueous solution when pH > 4.09 (Fig. 9(b)). As revealed by the speciation diagram of BPA molecule ($\text{pK}_a = 10.2$) (Bautista-Toledo et al., 2005), the undissociated Bis(OH)² was the dominating compound when pH < pK_a , while Bis(OH)(O)⁻ and Bis(O)²⁻ were prevalently existed in the solution when pH > pK_a . Therefore, it can be concluded that the electrostatic attraction between BM200 and BPA was stronger at pH = 3.0 and 11.0. Furthermore, the inhibiting effect tended to occur when pH = 11.0 owing to the electrostatic attraction effect between BM200 and $\text{S}_2\text{O}_8^{2-}$ anions, thus the adsorption capacity of BM200 to BPA was the highest when pH being 3.0. In general, $\text{SO}_4^{\cdot-}$ radical was inclined to generate under acidic environment according to Eqs. (14)–(15) (Lin et al., 2020). Nevertheless, $\text{SO}_4^{\cdot-}$ can also be transformed into SO_4^{2-} ions and $\bullet\text{OH}$ under alkaline environment (Eq. (7)). Considering that the $\text{SO}_4^{\cdot-}$ demonstrates a higher oxidizing potential ($\text{SO}_4^{\cdot-}$: 2.6–3.1 V vs $\bullet\text{OH}$: 1.8–2.7 V) and

possesses a longer half-life ($\text{SO}_4^{\cdot-}$: 30–40 μs vs $\bullet\text{OH}$: < 1 μs) (Wang et al., 2019a), the photocatalytic reaction rate over BM200/light/PS system under acidic condition was relatively faster, and the k values followed the order of pH = 3.0 ($0.15322 \pm 0.015358 \text{ min}^{-1}$) > pH = 5.2 ($0.14713 \pm 0.007821 \text{ min}^{-1}$) > pH = 7.0 ($0.09581 \pm 0.000863 \text{ min}^{-1}$) > pH = 9.0 ($0.06037 \pm 0.002758 \text{ min}^{-1}$) > pH = 11.0 ($0.05213 \pm 0.002503 \text{ min}^{-1}$). Moreover, the concentrations of the leached Fe ions under different initial solution pH were also analyzed in this study. The ICP-OES (ICP-5000, Focused Photonics (Hangzhou) Inc.) data showed that the concentrations of the leached Fe ions were 5.0384 ± 0.2285 , 3.5494 ± 0.3317 , 2.6216 ± 0.5237 , 1.6865 ± 0.5411 and $0.0168 \pm 0.0006 \text{ mg/L}$ for pH being 3.0, 5.2, 7.0, 9.0 and 11.0, respectively. The high content of leached Fe at pH = 3.0 may be related to homogeneous Fenton-like process and it was beneficial to the rapid oxidation of BPA. This phenomenon was in consistent with previous reports about the decomposition of organic pollutants based on PS-activation methods (Gao et al., 2017; Wang et al., 2019b). Besides, previous studies have proved that the dissolved Fe^{3+} can be photoreduced to Fe^{2+} under UV light ($\lambda < 360 \text{ nm}$) without any catalyst or reductant (Giannakis et al., 2016a; Giannakis et al., 2016b; Kim et al., 2019). Considering the spectral range of white light used in this study was approximately 340–660 nm (Fig. S1), so the more photo-induced $\text{Fe}^{3+}/\text{Fe}^{2+}$ redox transformations were also beneficial to PS activation, thus enhancing the BPA degradation efficiency. From another point of view, the MIL-100(Fe) was not remarkably stable under alkaline conditions (Kholdeeva et al., 2014), and Fe^{2+} tended to react with H_2O molecules, possible reactions were listed in Eqs. (16)–(17). To sum up, treating wastewater containing BPA without pre-adjusting the solution pH was the prominent advantage of the BM200/light/PS system.



3.2.2.2. Effect of PS dosage on BPA degradation. It is well known that the PS concentration can affect the degradation process due to that it is directly relevant to production of free radicals, such as $\text{SO}_4^{\cdot-}$ and $\bullet\text{OH}$ (Wei et al., 2020). As illustrated in Fig. 10(a), when the PS dosage increased from 0.1 to 2.0 mM, the removal rate was observed to distinctly accelerate. But the corresponding rate immediately reached to a plateau when the PS dosage was 4.0 mM. Meanwhile, the k values followed the

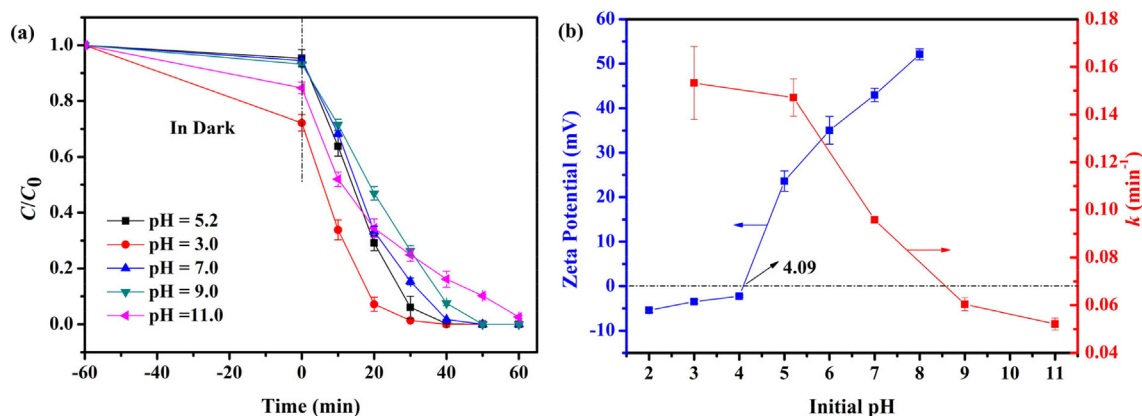


Fig. 9. (a) The photocatalytic degradation curves toward BPA and (b) the corresponding zeta potentials (blue line) and k values (red line) at different pH values. Condition: BM200 dosage = 0.25 g/L, BPA = 10 mg/L, PS = 0.2 mM. (For interpretation of the references to colour in this figure legend, the reader is referred to the web version of this article.)

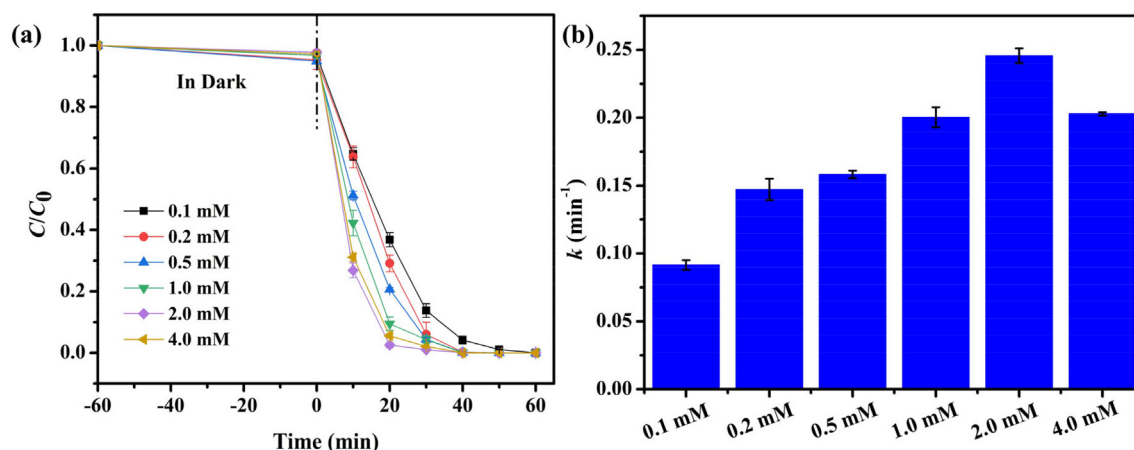
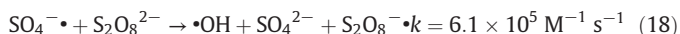


Fig. 10. (a) Effect of PS dosage on the BPA degradation and (b) the corresponding k values over the BM200/light/PS system. Condition: BM200 dosage = 0.25 g/L, BPA = 10 mg/L, pH = 5.2.

order of 2.0 mM ($0.24563 \pm 0.005452 \text{ min}^{-1}$) > 4.0 mM ($0.20276 \pm 0.001131 \text{ min}^{-1}$) > 1.0 mM ($0.20022 \pm 0.007474 \text{ min}^{-1}$) > 0.5 mM ($0.15822 \pm 0.002828 \text{ min}^{-1}$) > 0.2 mM ($0.14713 \pm 0.007821 \text{ min}^{-1}$) > 0.1 mM ($0.09141 \pm 0.003500 \text{ min}^{-1}$) (Fig. 10 (b)). The above experimental phenomenon can be ascribed to two reasons. Firstly, the yield of photo-generated carriers was constant for a given amount of photocatalyst and specific photon output, which might lead to the excess PS cannot be deemed as electron acceptors during the photocatalysis process, thus the photodegradation efficiency attained a stable plateau according to Eq. (6). Secondly, when the PS dosage was above 4.0 mM, the reactions might occur as expressed by the Eqs. (18)–(19). It is a remarkable fact that $\text{S}_2\text{O}_8^{\cdot-}$ is less reactive than $\text{SO}_4^{\cdot-}$, therefore, self-scavenging of $\text{SO}_4^{\cdot-}$ radicals was the main reason why the BPA removal rate decreased with the increase of $\text{S}_2\text{O}_8^{2-}$ dosage.



3.2.2.3. Effect of inorganic anions on BPA degradation. Inorganic anions are usually present in different water environments and might dramatically affect the degradation efficiency of organic pollutants. Therefore, to further investigate the practical applications of the BM200/light/PS system, the BPA degradation was determined with the addition of inorganic

anions, such as H_2PO_4^- , HCO_3^- , SO_4^{2-} , NO_3^- and Cl^- . As illustrated in Fig. 11(a)–(b), all the inorganic anions had detrimental effects on the BPA degradation, resulting in the k values followed the order of no anions ($0.14713 \pm 0.007821 \text{ min}^{-1}$) > NO_3^- ($0.05482 \pm 0.009496 \text{ min}^{-1}$) > Cl^- ($0.04656 \pm 0.010331 \text{ min}^{-1}$) > SO_4^{2-} ($0.03686 \pm 0.011434 \text{ min}^{-1}$) > H_2CO_3^- ($0.02924 \pm 0.007707 \text{ min}^{-1}$) > H_2PO_4^- ($0.014695 \pm 0.003260 \text{ min}^{-1}$). It was obvious that the H_2PO_4^- and HCO_3^- displayed significant inhibiting effects on BPA degradation, the corresponding efficiencies decreased to 65.4% and 85.8%, respectively. It is well-known that the H_2PO_4^- usually acts as radical scavengers in different AOPs, the inhibition for the BPA degradation by H_2PO_4^- can be attributed to its competing reactions with h^+ and $\cdot\text{OH}$ (Eqs. (20)–(21)), in which the generated $\text{H}_2\text{PO}_4^{\cdot}$ was less active than h^+ and $\cdot\text{OH}$ (Wang et al., 2017b; Zhao et al., 2018a). As far as HCO_3^- , it has been reported that HCO_3^- would compete for $\cdot\text{OH}$ and $\text{SO}_4^{\cdot-}$ to produce weak free radicals (HCO_3^{\cdot} and $\text{CO}_3^{\cdot-}$) as expressed by Eqs. (22)–(23) (Ghauch and Tuqan, 2012; Lin et al., 2020). Although SO_4^{2-} could exert moderate inhibiting effect on BPA degradation in BM200/light/PS system, 93.8% of BPA still could be removed within 120 min. This might be ascribed to that both the $\text{S}_2\text{O}_8^{\cdot-}$ and $\text{SO}_4^{\cdot-}$ could be scavenged by the excess sulfate (Wang and Liang, 2014). However, Cl^- and NO_3^- displayed the relatively weak inhibiting effect on the BPA degradation under the same experimental conditions, namely 96.1% and 96.4% of BPA could be removed within 120 min, respectively. Normally, the Cl^- and NO_3^- are inclined to react with $\text{SO}_4^{\cdot-}$ and $\cdot\text{OH}$ to form less-reactive radicals (Cl^{\cdot} , $\text{Cl}_2^{\cdot-}$ and NO_3^{\cdot}) as expressed by Eqs. (24)–(28)

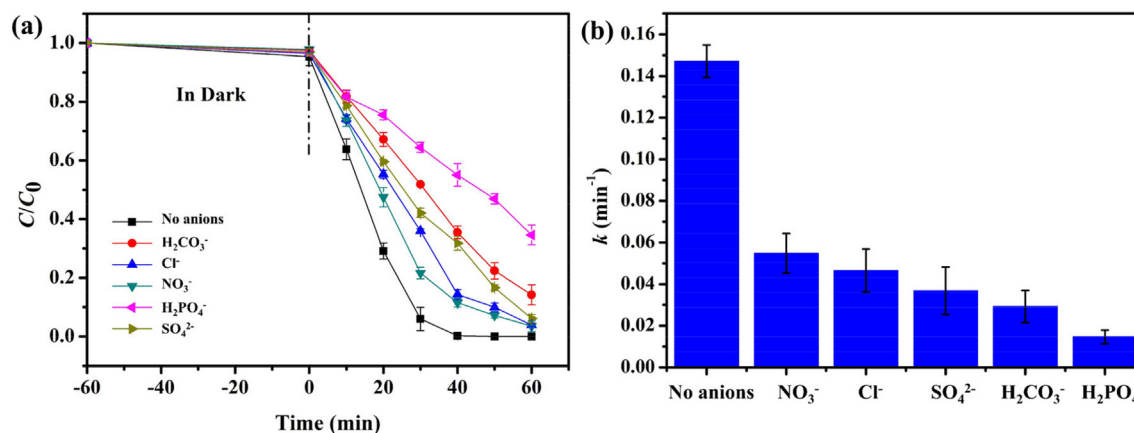
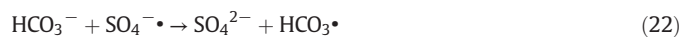


Fig. 11. (a) Effect of inorganic anions on the BPA degradation and (b) the corresponding k values over the BM200/light/PS system. Condition: BM200 dosage = 0.25 g/L, BPA = 10 mg/L, pH = 5.2, PS = 0.2 mM, anions = 1.0 mM.

(Dugandžić et al., 2017; Wang et al., 2018; Yuan et al., 2019), which can also induce the BPA decomposition process.



3.3. Reusability and stability of BMx composites

The long-term recyclability and stability of a catalyst are imperative for the actual applications. In this work, the recycling usability of the BM200 in photoreduction of Cr(VI) and degradation of BPA was explored. As illustrated in Fig. 12(a)–(b), there was no evident decrease in the catalytic efficiencies for both the Cr(VI) removal and BPA decomposition after five recycles under the optimal conditions. Furthermore, the k values were even 0.02418 and 0.05372 min^{−1} for Cr(VI) reduction

and BPA degradation in the corresponding fifth cycle, respectively (Fig. S7). Moreover, the PXRD patterns and FTIR spectra of the BM200 before and after the catalysis revealed that the chemical constitution and crystalline structure of the BM200 still kept unchanged even after five cycles (Fig. 12(c)–(d)). Additionally, according to the HRTEM images before and after the catalytic reactions (Fig. S8(a)–(b)), the BM200 also maintained its original morphology. Therefore, the above results confirmed that the BM200 possessed powerful stability and can be deemed as an excellent candidate for cyclic treatment of Cr(VI)- and BPA-containing wastewater.

3.4. Possible mechanism for the photocatalytic reaction

To gain a clear idea of the generation and transfer mechanism of the photo-generated carriers, PL spectra, Nyquist impedance plots and photocurrent analysis were investigated in this study. Fig. 13(a) displayed the PL spectra, it was obvious that the photoluminescence intensity of the as-prepared materials confirmed to the following order: MIL-100(Fe) > Bi₁₂O₁₇Cl₂ > BM100 > BM500 > BM400 > BM300 > BM200, indicating that the BM200 possessed the longest lifetime of photo-generated carriers (Chen et al., 2020; Yi et al., 2019; Zhao et al., 2020). Fig. 13(b) showed the EIS Nyquist plots, BMx composites owned the smaller arc radius than the pristine MIL-100(Fe) and Bi₁₂O₁₇Cl₂, meaning that the fabrication of composites between MIL-100(Fe) and Bi₁₂O₁₇Cl₂ was conducive to suppress the photo-generated carriers recombination (Chen et al., 2020; Yi et al., 2019; Zhao et al., 2020). From another point of view, the photocurrent-time curves for the MIL-100(Fe), Bi₁₂O₁₇Cl₂ and BM200 were illustrated in Fig. 13(c). It can be found that the whole of materials can immediately produce photocurrent and the photocurrent remained steady after light on/off cycles. As we all know, the higher photocurrent value corresponds the quicker

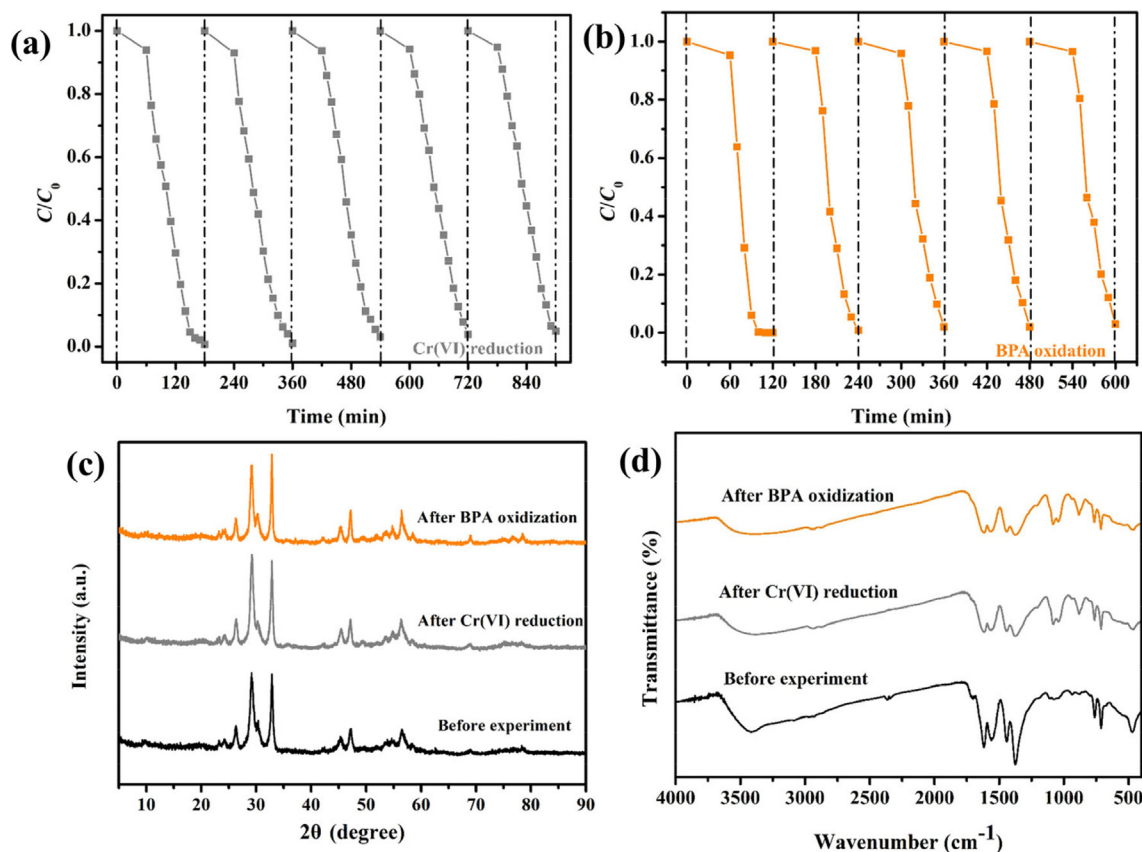


Fig. 12. Reusability tests with BM200 for (a) Cr(VI) reduction (condition: BM200 dosage = 0.5 g/L, Cr(VI) = 10.0 mg/L, pH = 2.0) and (b) BPA degradation (condition: BM200 dosage = 0.25 g/L, BPA = 10.0 mg/L, pH = 5.2, PS = 0.2 mM), (c)–(d) PXRD patterns and FTIR spectra of the BM200 before and after the cyclic experiments.

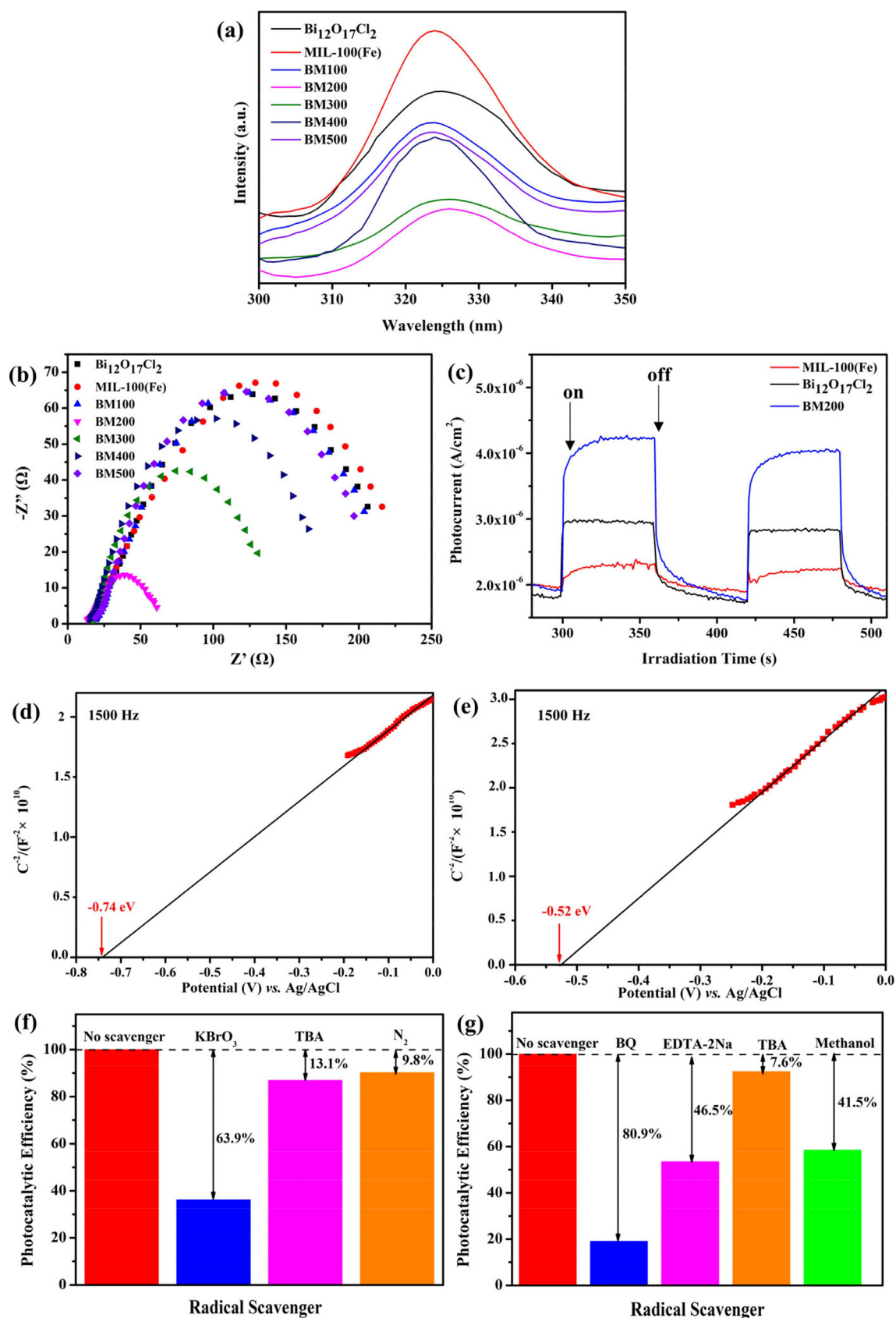


Fig. 13. (a) Photoluminescence spectra, (b) Nyquist impedance plots, (c) transient photocurrent responses of the as-prepared photocatalysts, (d)–(e) Mott-Schottky plots of MIL-100 (Fe) and $\text{Bi}_{12}\text{O}_{17}\text{Cl}_2$, (f) effect of various quenching scavengers on Cr(VI) removal over BM200/light system and (g) reactive species trapping experiments for BPA degradation over BM200/light/PS system.

transfer rate of photo-generated carriers (Wang et al., 2016). The photocurrent density of the BM200 was calculated to be 4.09 μA , which was about 1.38 and 1.82 times as compared with that of pristine $\text{Bi}_{12}\text{O}_{17}\text{Cl}_2$ and MIL-100(Fe), suggesting more remarkable separation efficiency and prolonged lifetime of photo-generated carriers in BMx composites.

To elucidate the main mechanism over the BMx composites, the valence state of the BM200 was determined by Mott-Schottky measurements. As shown in Fig. 13(d)-(e), the flat-band potentials (E_{FB}) of $\text{Bi}_{12}\text{O}_{17}\text{Cl}_2$ and MIL-100(Fe) were about -0.74 and -0.52 eV vs. Ag/AgCl electrode, respectively. Moreover, the slopes of linear C^{-2} potential curve of $\text{Bi}_{12}\text{O}_{17}\text{Cl}_2$ and MIL-100(Fe) were positive, revealing that $\text{Bi}_{12}\text{O}_{17}\text{Cl}_2$ and MIL-100(Fe) were n-typed semiconductors (Sun et al., 2006). It is well established that the E_{FB} potential is more positive 0.1 eV than the conduction band (E_{CB}) potential for the large number of n-typed semiconductor (Zhao et al., 2020), hence the E_{CB} of $\text{Bi}_{12}\text{O}_{17}\text{Cl}_2$ and E_{LUMO} of MIL-100(Fe) were -0.64 and -0.42 eV vs. NHE. Combining with the E_g values calculated from UV-vis DRS spectra, the E_{VB} of $\text{Bi}_{12}\text{O}_{17}\text{Cl}_2$ and the E_{HOMO} of MIL-100(Fe) were calculated to be 1.41 and 2.40 eV vs. NHE.

In this study, active-species-trapping experiments were carried out to fully understand the photocatalytic processes. With respect to Cr(VI) reduction, KBrO_3 and *t*-butanol (TBA) were employed as scavengers to quench e^- and $\bullet\text{OH}$ species, respectively. As illustrated in Fig. 13(f), about 63.9% suppression can be observed when KBrO_3 was added to the photocatalytic system, manifesting that dominating role of photo-generated e^- for Cr(VI) reduction. The inhibitory effect of TBA (13.1%) suggested that the photo-generated $\bullet\text{OH}$ was also responsible for Cr(VI) removal, since capture of $\bullet\text{OH}$ was in favor of the equilibrium shifting toward Cr(VI) as reported by our previous studies (Yi et al., 2019; Zhao et al., 2020). Moreover, the Cr(VI) reduction was suppressed in N_2 ambient, the Cr(VI) removal efficiency decreased by 9.8% in N_2 ambient compared with 100.0% reduction in air after 120 min photoreaction. This phenomenon implied that O_2 also contributed to the Cr(VI) reduction, since the photo-generated electrons were usually scavenged by O_2 to yield $\bullet\text{O}_2^-$, which had been proved to be a mediator for Cr(VI) reduction (Chen et al., 2020; Yi et al., 2019; Zhao et al., 2020).

In terms of the degradation of BPA over BM200/light/PS system, BQ and EDTA-2Na were selected as scavengers to quench $\bullet\text{O}_2^-$ and h^+ radicals. Considering that the $\bullet\text{OH}$ and $\text{SO}_4^{\bullet-}$ can be quenched by methanol through similar reaction rates (Zeng et al., 2015), the constant of reaction rate for TBA changes from $3.8 \times 10^8 \text{ M}^{-1} \text{ s}^{-1}$ to $7.6 \times 10^8 \text{ M}^{-1} \text{ s}^{-1}$ for $\bullet\text{OH}$, and varies from $4.0 \times 10^5 \text{ M}^{-1} \text{ s}^{-1}$ to $9.1 \times 10^5 \text{ M}^{-1} \text{ s}^{-1}$ for $\text{SO}_4^{\bullet-}$ (Liang and Su, 2009; Sharma et al., 2015b),

implying that TBA had approximately three orders of magnitude higher rate of scavenging $\bullet\text{OH}$ than that for $\text{SO}_4^{\bullet-}$ radicals. Therefore, TBA was used to scavenge $\bullet\text{OH}$ radicals and methanol was selected as the scavenger of both $\bullet\text{OH}$ and $\text{SO}_4^{\bullet-}$ in this study. As illustrated in Fig. 13(g), the corresponding catalytic efficiency decreased by 80.9% with the existence of BQ, indicating that the $\bullet\text{O}_2^-$ was a major radical during the photocatalytic process. Furthermore, 46.5% suppression can be observed with the presence of EDTA-2Na, suggesting that h^+ species were also responsible for BPA degradation in the BM200/light/PS system. It was worth noting that the inhibition effect with the existence of methanol (41.5%) was obviously stronger than that with TBA (7.6%), revealing that the $\text{SO}_4^{\bullet-}$ was an important radical in this case. In general, the aforementioned reactions might cooperatively contribute to the degradation efficiency of BPA molecules.

Based on the aforementioned discussion, the plausible mechanisms for Cr(VI) reduction and BPA degradation were presented in Fig. 14. With respect to Cr(VI) reduction (Fig. 14(a)), the photo-generated electrons and holes were bound to produce on $\text{Bi}_{12}\text{O}_{17}\text{Cl}_2$ and $\text{Fe}_3\text{-}\mu_3\text{-oxo}$ clusters in MIL-100(Fe) through ligand to metal charge transfer (LMCT) process under white light illumination (Wang et al., 2017a; Xu et al., 2017). Consequently, the photo-excited electrons from the CB of $\text{Bi}_{12}\text{O}_{17}\text{Cl}_2$ were moved to the LUMO of MIL-100(Fe) (-0.42 eV vs. NHE), which was more negative than Cr(VI)/Cr(III) potential ($+0.51$ eV vs. NHE) (Huang et al., 2017). Therefore, the reaction process from Cr(VI) to Cr(III) through the electrons was thermodynamically feasible. Furthermore, because the E_{LUMO} of MIL-100(Fe) (-0.42 eV vs. NHE) were much more negative than the potential of $\text{O}_2/\bullet\text{O}_2^-$ (-0.33 eV vs. NHE), so the free electrons might partly react with O_2 to generate $\bullet\text{O}_2^-$, which was also responsible for Cr(VI) reduction (Chen et al., 2020; Yi et al., 2019; Zhao et al., 2020). More importantly, the remaining holes in the HOMO of MIL-100(Fe) were inclined to migrate to the VB of $\text{Bi}_{12}\text{O}_{17}\text{Cl}_2$, resulting in decreasing the opportunity of photo-generated carriers recombination and harvest more electrons in the LUMO of MIL-100(Fe). Meanwhile, the accumulated holes were inclined to oxidize the SOAs to generate CO_2 and H_2O , so the addition of the above green SOAs can further enhance the photoreduction activity over BM200 in our reaction system.

As for the BPA degradation (Fig. 14(b)), the photo-generated electrons in LUMO of MIL-100(Fe) can reduce the adsorbed O_2 to produce $\bullet\text{O}_2^-$, which can rapidly decompose BPA molecules. However, the improved BPA degradation rate should be ascribed to the scavenging of the photo-generated electrons in LUMO of MIL-100(Fe) via introducing the electron acceptor of PS, which can efficiently suppress the recombination of photo-generated charge carriers and promote the productions

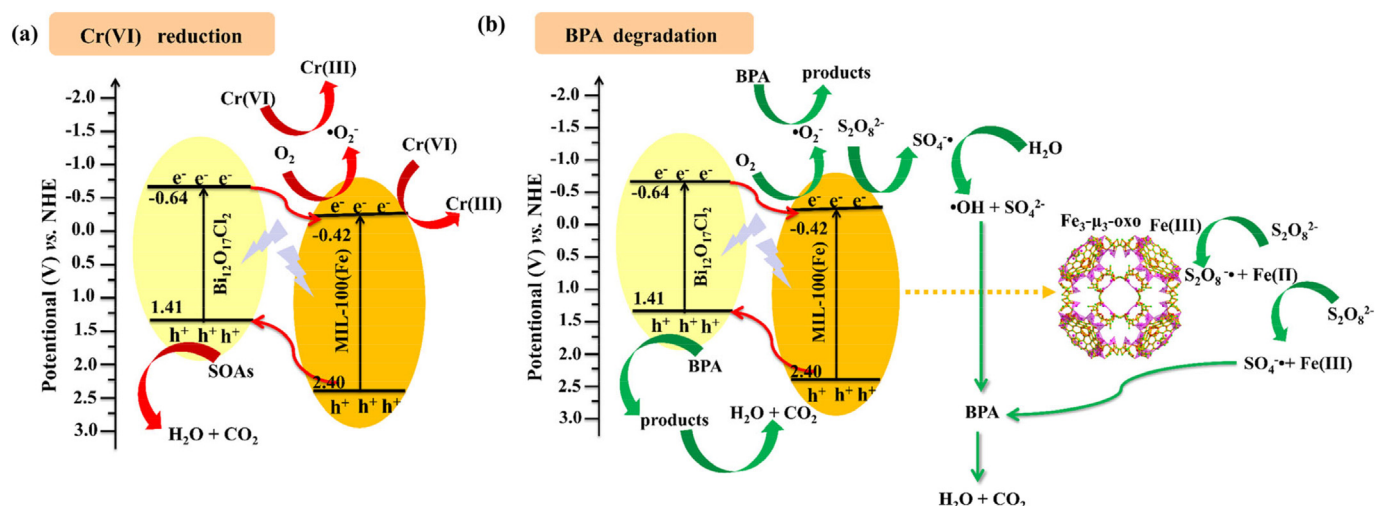


Fig. 14. The possible mechanisms for (a) Cr(VI) reduction and (b) BPA decomposition over BM200 under white light illumination.

of $\text{SO}_4^{\bullet-}$ and $\bullet\text{OH}$ radicals (Eqs. (6) and (7)). The above two O-containing radicals with strong oxidizability can rapidly photodegrade BPA molecules. Additionally, the $\text{Fe}_3\text{-}\mu_3\text{-oxo}$ clusters on the surface of BM200 were beneficial to trigger the PS activation reaction to generate $\text{SO}_4^{\bullet-}$ radicals by the Fenton-like process (Eqs. (9) and (10)). It was also believed that some holes would directly oxidize the BPA. As a result, the BM200 composite displayed prominent catalytic activity for BPA decomposition assisted by PS.

3.5. BPA degradation pathway and DFT calculation

Theoretical DFT calculation was applied to understand the precise degradation pathway of BPA. Fig. 15 showed the nucleophilic (f^-) and electrophilic attack (f^+) values of BPA molecule represented by Fukui index according to natural population analysis (NPA). Previous studies had proved that the HOMO and LUMO orbitals can describe the easy loss or gain of electrons on each BPA molecule site during the photocatalytic process, respectively (Zhao et al., 2018b). As illustrated in Fig. 15 (b), the purple surface represented the electron-rich region and the light blue surface represented the electron-deficient region. Therefore, the symmetrical phenyl rings were easy to escape electrons and will be attacked by $\bullet\text{OH}/\bullet\text{O}_2^-/\text{SO}_4^{\bullet-}$ nucleophilic radicals. Meanwhile, the counterpoint carbon atoms of the phenolic hydroxyl were inclined to gain electrons and might be attacked by h^+ electrophilic radical. In this study, the shade intensities of the red boxes in Fig. 15 (c) exhibited different levels of f^- and f^+ . Therefore, the results suggested that the C_1 , C_3 , C_{10} and C_{14} (highlighted in red in Fig. 15(a)) with high values will be the active sites where free radicals were most likely to attack. Based on the catalytic products affirmed by UHPLC-MS and DFT calculation analysis, the credible BPA degradation pathway was proposed in Fig. 16. There were three major pathways for BPA degradation: (1) $\bullet\text{O}_2^-/\bullet\text{OH}$ addition (blue line), (2) h^+ attacking to $\text{C}_7\text{-C}_3$ or $\text{C}_7\text{-C}_{10}$ cleavage (red line), and (3) $\text{SO}_4^{\bullet-}$ induced hydroxylation process (green line). At first, $\bullet\text{OH}$ radicals preferred to attack on C_1 and C_{14} , leading to generate dihydroxylated BPA (B, $m/z = 259$), which was consistent with previous studies (Subagio et al., 2010; Zhao et al., 2018b). Meanwhile, the presence of $\bullet\text{O}_2^-$ radicals were inclined to attack the aromatic rings via the nucleophilic effect, which was responsible for a series of multihydroxylation processes. Subsequently, the C—C bond of BPA between benzene rings and isopropyl was ruptured by $\bullet\text{OH}$ radicals to form intermediate C ($m/z = 151$), which might rapidly transform into 2-isopropylmuconic acid (D, $m/z = 183$) after a specific ring-

open process. Secondly, C_3 and C_{10} showed the highest f^- values of 0.09524, indicating that the above two C positions were highly vulnerable to electrophilic attack. Therefore, it was ruptured by photo-generated h^+ with the formation of 4-isopropenylphenol radicals (compound E) and phenol (F, $m/z = 93$). Then the 4-isopropenylphenol radicals were inclined to form the stable 4-isopropenylphenol molecules (G, $m/z = 133$), which can be further oxidized to form 4'-hydroxyacetophenone (H, $m/z = 135$) through Fenton-like process (Molkenthin et al., 2013). Additionally, the attack of $\bullet\text{OH}$ radicals on compound E and F may also produce the same intermediate C. The third pathway was led by $\text{SO}_4^{\bullet-}$ oxidation. When the $\text{SO}_4^{\bullet-}$ radicals attacked the BPA molecules, one electron was transferred from the BPA molecule to generate C-centered BPA cationic radical. Then, this cationic radical underwent hydrolytic process to form OH adducts ($\text{OH}(\text{BPA}^+)$ or $(\text{OH})_2(\text{BPA}^+)$) (Sharma et al., 2015a; Sharma et al., 2016), which were further oxidized to dihydroxylated BPA (compound B, $m/z = 259$). Then, the generated compound B was more likely to be oxidized to quinone of dihydroxylated BPA (I, $m/z = 257$) (Sharma et al., 2015a; Sharma et al., 2016). Overall, the catalytic intermediates can further decompose to low molecular weight compounds, such as short chain aliphatic acids and mineralization products of CO_2 and H_2O .

4. Conclusions

Bifunctional BMx composites were firstly prepared by a facile ball-milling method, where MIL-100(Fe) acted as the substrate for the construction of BMx composites. As expected, the as-prepared composites were effective not only toward photoreduction of Cr(VI) but also for the degradation of BPA with addition of PS in aquatic environment under the white light illumination. Being compared to the pristine $\text{Bi}_{12}\text{O}_{17}\text{Cl}_2$ and MIL-100(Fe), the BMx composites showed improved catalytic performances for both the Cr(VI) reduction and BPA degradation reactions. The results of photoelectrochemical analysis and PL spectra suggested that the construction of BMx composites was beneficial to facilitate the transfer and migration of photo-generated charge carriers, which contributed significantly to improve the final catalytic efficiencies. Furthermore, DFT calculation and UHPLC-MS analysis indicated that both nucleophilic and electrophilic attack can describe the active sites of BPA over BM200/light/PS system. Meanwhile, cyclic experiments also suggested that the BMx composites had reasonable outstanding reusability and stability in removing Cr(VI)- and PPCPs-containing wastewater. This research will arouse intense attentions to forcefully strengthen the photocatalytic

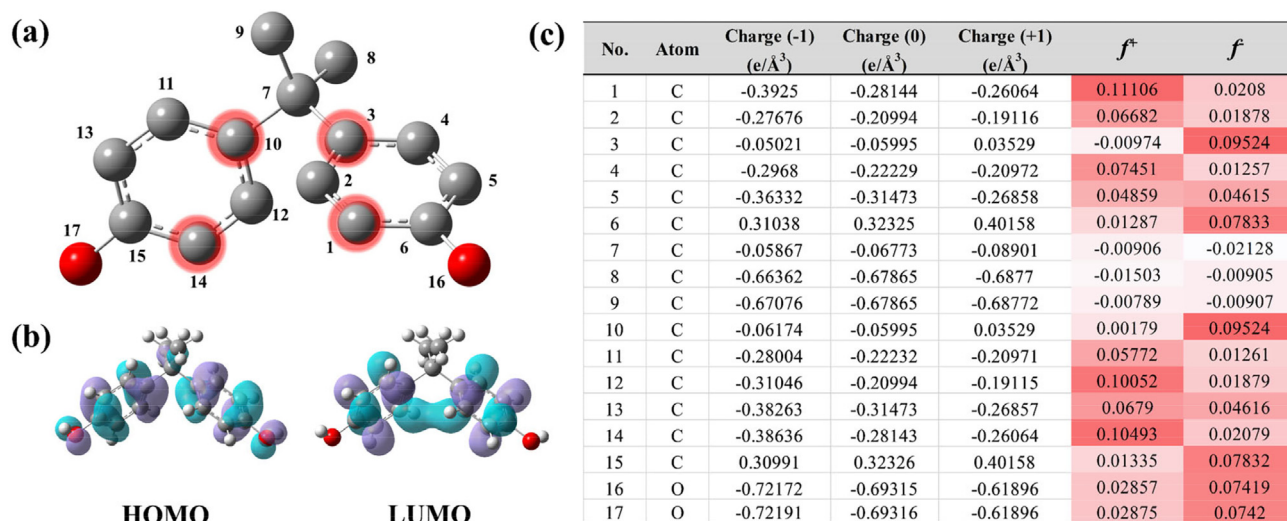


Fig. 15. (a) Chemical structure, (b) HOMO and LUMO orbitals and (c) NPA charge distribution and Fukui indexes of BPA.

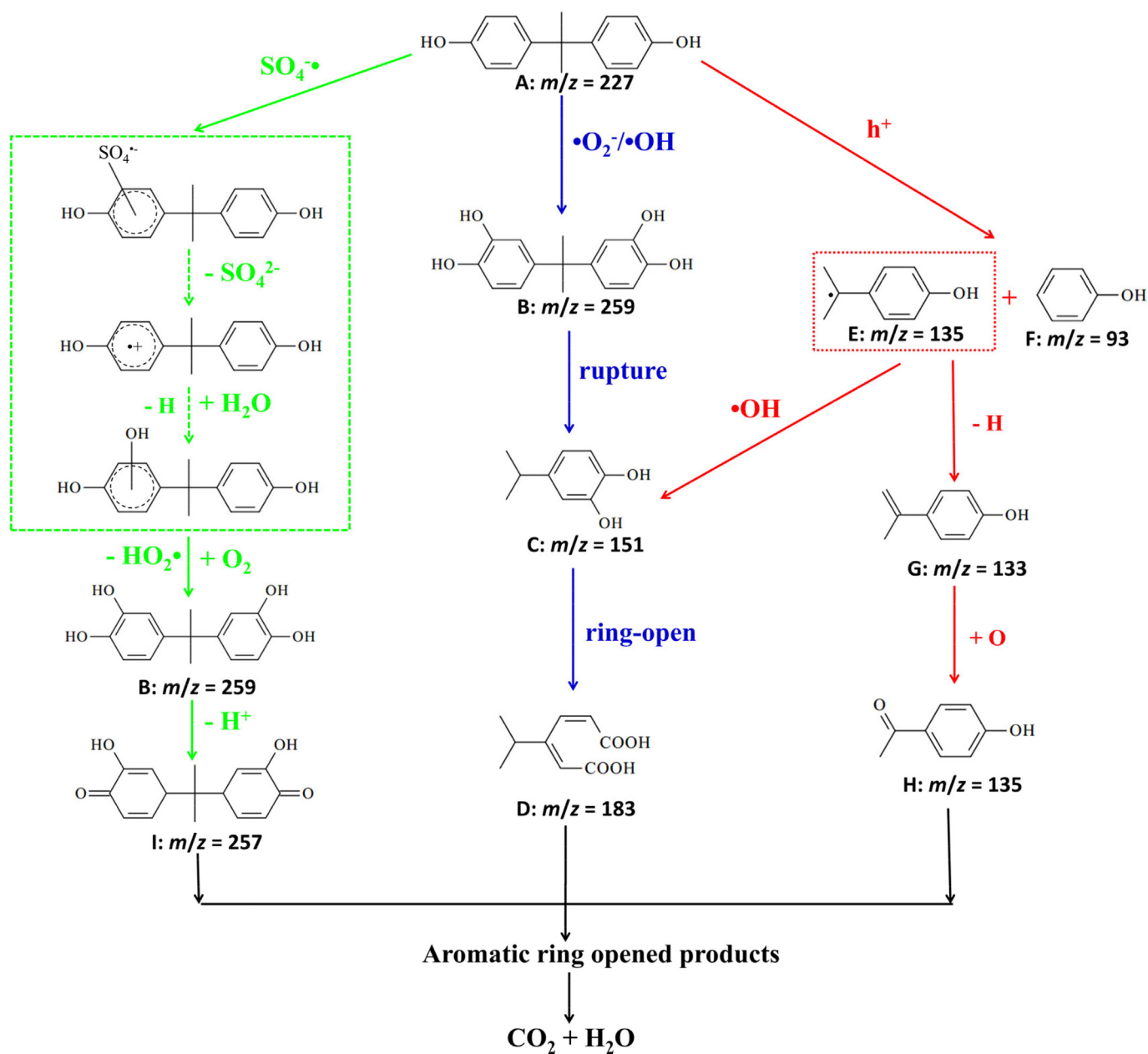


Fig. 16. Proposed BPA degradation pathway over BM200/light/PS system.

activity of MOFs-based materials by coupling bismuth-rich bismuth oxyhalides ($\text{Bi}_x\text{O}_y\text{X}_z$, X = Cl, Br and I).

CRedit authorship contribution statement

Chen Zhao: Data curation, Investigation, Visualization, Writing - Original draft preparation.

Jiasheng Wang: Resources, Investigation, Instrumental.

Xi Chen: Resources, Instrumental.

Zhihua Wang: Funding acquisition, Supervision, Project administration.

Haodong Ji: Software, Validation.

Long Chen: Instrumental.

Wen Liu: Resources, Software, Validation.

Chong-Chen Wang: Conceptualization, Funding acquisition, Supervision, Project administration, Writing - review & editing.

Declaration of competing interest

On behalf of all authors, I declare that we do not have any commercial or associative interest that represents a conflict of interest in connection with the work entitled "Bifunctional $\text{Bi}_{12}\text{O}_{17}\text{Cl}_2/\text{MIL-100}(\text{Fe})$ composites toward photocatalytic Cr(VI) sequestration and activation of persulfate for bisphenol A degradation".

Acknowledgements

This work was supported by the National Natural Science Foundation of China (21876008 and 51878023), Beijing Natural Science Foundation (No. 8202016), Great Wall Scholars Training Program Project of Beijing Municipality Universities (CIT&TCD20180323), Beijing Talent Project (2019A22), the Fundamental Research Funds for Beijing Universities (X18075/X18076/X18124/X18125/X18276) and Scientific

Research Foundation of Beijing University of Civil Engineering and Architecture (KYJJ2017033/KYJJ2017008).

Appendix A. Supplementary data

Supplementary data to this article can be found online at <https://doi.org/10.1016/j.scitotenv.2020.141901>.

References

- Bautista-Toledo, I., Ferro-García, M.A., Rivera-Utrilla, J., Moreno-Castilla, C., Vegas Fernández, F.J., 2005. Bisphenol A removal from water by activated carbon. Effects of carbon characteristics and solution chemistry. *Environ. Sci. Technol.* 39, 6246–6250.
- Bolisetty, S., Peydayesh, M., Mezzenga, R., 2019. Sustainable technologies for water purification from heavy metals: review and analysis. *Chem. Soc. Rev.* 48, 463–487.
- Cedeño, E., Cabrera, H., Delgadillo-López, A.E., Delgado-Vasallo, O., Mansanares, A.M., Calderón, A., Marín, E., 2017. High sensitivity thermal lens microscopy: Cr-VI trace detection in water. *Talanta* 170, 260–265.
- Chang, F., Wu, F., Zheng, J., Cheng, W., Yan, W., Deng, B., Hu, X., 2018. In-situ establishment of binary composites $\alpha\text{-Fe}_2\text{O}_3/\text{Bi}_{12}\text{O}_{17}\text{Cl}_2$ with both photocatalytic and photo-Fenton features. *Chemosphere* 210, 257–266.
- Chen, D.-D., Yi, X.-H., Zhao, C., Fu, H., Wang, P., Wang, C.-C., 2020. Polyaniline modified MIL-100(Fe) for enhanced photocatalytic Cr(VI) reduction and tetracycline degradation under white light. *Chemosphere* 245, 125659.
- Di, J., Xia, J., Ji, M., Li, H., Xu, H., Li, H., Chen, R., 2015. The synergistic role of carbon quantum dots for the improved photocatalytic performance of Bi_2MoO_6 . *Nanoscale* 7, 11433–11443.
- Ding, J., Yang, Z., He, C., Tong, X., Li, Y., Niu, X., Zhang, H., 2017. $\text{UiO}-66(\text{Zr})$ coupled with Bi_2MoO_6 as photocatalyst for visible-light promoted dye degradation. *J. Colloid Interf. Sci.* 497, 126–133.
- Du, X., Yi, X., Wang, P., Deng, J., Wang, C.-C., 2019. Enhanced photocatalytic Cr(VI) reduction and diclofenac sodium degradation under simulated sunlight irradiation over MIL-100(Fe)/g- C_3N_4 heterojunctions. *Chinese J. Catal.* 40, 70–79.
- Du, X., Bai, X., Xu, L., Yang, L., Jin, P., 2020. Visible-light activation of persulfate by $\text{TiO}_2/\text{g-}\text{C}_3\text{N}_4$ photocatalyst toward efficient degradation of micropollutants. *Chem. Eng. J.* 384, 123245.
- Dugandžić, A.M., Tomašević, A.V., Radišić, M.M., Šekuljica, N.Ž., Mijin, D.Ž., Petrović, S.D., 2017. Effect of inorganic ions, photosensitisers and scavengers on the photocatalytic degradation of nicosulfuron. *J. Photoch. Photobio. A* 336, 146–155.
- Gao, Y., Li, S., Li, Y., Yao, L., Zhang, H., 2017. Accelerated photocatalytic degradation of organic pollutant over metal-organic framework MIL-53(Fe) under visible LED light mediated by persulfate. *Appl. Catal. B-Environ.* 202, 165–174.
- Ghauch, A., Tuqan, A.M., 2012. Oxidation of bisoprolol in heated persulfate/ H_2O systems: kinetics and products. *Chem. Eng. J.* 183, 162–171.
- Giannakis, S., López, M.I.P., Spuhler, D., Pérez, J.A.S., Ibáñez, P.F., Pulgarin, C., 2016a. Solar disinfection is an augmentable, in situ-generated photo-Fenton reaction—part 2: a review of the applications for drinking water and wastewater disinfection. *Appl. Catal. B-Environ.* 198, 431–446.
- Giannakis, S., Polo López, M.I., Spuhler, D., Sánchez Pérez, J.A., Fernández Ibáñez, P., Pulgarin, C., 2016b. Solar disinfection is an augmentable, in situ-generated photo-Fenton reaction—part 1: a review of the mechanisms and the fundamental aspects of the process. *Appl. Catal. B-Environ.* 199, 199–223.
- Gong, Y., Yang, B., Zhang, H., Zhao, X., 2018. A g- C_3N_4 /MIL-101(Fe) heterostructure composite for highly efficient BPA degradation with persulfate under visible light irradiation. *J. Mater. Chem. A* 6, 23703–23711.
- He, G., Xing, C., Xiao, X., Hu, R., Zuo, X., Nan, J., 2015. Facile synthesis of flower-like $\text{Bi}_{12}\text{O}_{17}\text{Cl}_2/\beta\text{-Bi}_2\text{O}_3$ composites with enhanced visible light photocatalytic performance for the degradation of 4-tert-butylphenol. *Appl. Catal. B-Environ.* 170–171, 1–9.
- Herrmann, H., 2007. On the photolysis of simple anions and neutral molecules as sources of $\text{O}^\bullet/\text{OH}$, $\text{SO}_4^{\bullet-}$ and Cl^\bullet in aqueous solution. *Phys. Chem. Chem. Phys.* 9, 3935–3964.
- Huang, W., Liu, N., Zhang, X., Wu, M., Tang, L., 2017. Metal organic framework g- C_3N_4 /MIL-53(Fe) heterojunctions with enhanced photocatalytic activity for Cr(VI) reduction under visible light. *Appl. Surf. Sci.* 425, 107–116.
- Ismail, L., Ferronato, C., Fine, L., Jaber, F., Chovelon, J.-M., 2017. Elimination of sulfaclozine from water with $\text{SO}_4^{\bullet-}$ radicals: evaluation of different persulfate activation methods. *Appl. Catal. B-Environ.* 201, 573–581.
- Jin, X., Ye, L., Xie, H., Chen, G., 2017. Bismuth-rich bismuth oxyhalides for environmental and energy photocatalysis. *Coord. Chem. Rev.* 349, 84–101.
- Karthikeyan, B., Udayabhaskar, R., Kishore, A., 2014. Optical and phonon properties of Sm-doped $\alpha\text{-Bi}_2\text{O}_3$ micro rods. *Appl. Phys. A Mater. Sci. Process.* 117, 1409–1414.
- Kholdeeva, O.A., Skobelev, I.Y., Ivanchikova, I.D., Kovalenko, K.A., Fedin, V.P., Sorokin, A.B., 2014. Hydrocarbon oxidation over Fe- and Cr-containing metal-organic frameworks MIL-100 and MIL-101—a comparative study. *Catal. Today* 238, 54–61.
- Kim, D.-H., Lee, D., Monllor-Satoca, D., Kim, K., Lee, W., Choi, W., 2019. Homogeneous photocatalytic $\text{Fe}^{3+}/\text{Fe}^{2+}$ redox cycle for simultaneous Cr(VI) reduction and organic pollutant oxidation: roles of hydroxyl radical and degradation intermediates. *J. Hazard. Mater.* 372, 121–128.
- Leusch, F.D.L., Neale, P.A., Busetti, F., Card, M., Humpage, A., Orbell, J.D., Ridgway, H.F., Stewart, M.B., van de Merwe, J.P., Escher, B.J., 2019. Transformation of endocrine disrupting chemicals, pharmaceutical and personal care products during drinking water disinfection. *Sci. Total Environ.* 657, 1480–1490.
- Liang, C., Su, H.-W., 2009. Identification of sulfate and hydroxyl radicals in thermally activated persulfate. *Ind. Eng. Chem. Res.* 48, 5558–5562.
- Lin, J., Hu, Y., Wang, L., Liang, D., Ruan, X., Shao, S., 2020. M88/PS/Vis system for degradation of bisphenol A: environmental factors, degradation pathways, and toxicity evaluation. *Chem. Eng. J.* 382, 122931.
- Matzek, L.W., Carter, K.E., 2016. Activated persulfate for organic chemical degradation: a review. *Chemosphere* 151, 178–188.
- Miao, S., Zha, Z., Li, Y., Geng, X., Yang, J., Cui, S., Yang, J., 2019. Visible-light-driven MIL-53(Fe)/BiOCl composite assisted by persulfate: Photocatalytic performance and mechanism. *J. Photoch. Photobio. A* 380, 111862.
- Molkenthin, M., Olmez-Hanci, T., Jekel, M.R., Arslan-Alaton, I., 2013. Photo-Fenton-like treatment of BPA: effect of UV light source and water matrix on toxicity and transformation products. *Water Res.* 47, 5052–5064.
- Sharma, J., Mishra, I.M., Dionysiou, D.D., Kumar, V., 2015a. Oxidative removal of Bisphenol A by UV-C/peroxymonosulfate (PMS): kinetics, influence of co-existing chemicals and degradation pathway. *Chem. Eng. J.* 276, 193–204.
- Sharma, J., Mishra, I.M., Kumar, V., 2015b. Degradation and mineralization of Bisphenol A (BPA) in aqueous solution using advanced oxidation processes: UV/ H_2O_2 and UV/ $\text{S}_2\text{O}_8^{2-}$ oxidation systems. *J. Environ. Manag.* 156, 266–275.
- Sharma, J., Mishra, I.M., Kumar, V., 2016. Mechanistic study of photo-oxidation of Bisphenol-A (BPA) with hydrogen peroxide (H_2O_2) and sodium persulfate (SPS). *J. Environ. Manag.* 166, 12–22.
- Shen, S., Chen, J., Koodali, R.T., Hu, Y., Xiao, Q., Zhou, J., Wang, X., Guo, L., 2014. Activation of MCM-41 mesoporous silica by transition-metal incorporation for photocatalytic hydrogen production. *Appl. Catal. B-Environ.* 150–151, 138–146.
- Song, G., Wang, Z., Wang, L., Li, G., Huang, M., Yin, F., 2014. Preparation of MOF(Fe) and its catalytic activity for oxygen reduction reaction in an alkaline electrolyte. *Chinese J. Catal.* 35, 185–195.
- Subagio, D.P., Srinivasan, M., Lim, M., Lim, T.-T., 2010. Photocatalytic degradation of bisphenol-A by nitrogen-doped TiO_2 hollow sphere in a vis-LED photoreactor. *Appl. Catal. B-Environ.* 95, 414–422.
- Sun, L.-P., Niu, S.-Y., Jin, J., Yang, G.-D., Ye, L., 2006. Crystal structure and surface photovoltage of a series of Ni(II) coordination supramolecular polymer. *Inorganic Chem. Commun.* 9, 679–682.
- Tang, Q., An, X., Lan, H., Liu, H., Qu, J., 2019. Polyoxometalates/ TiO_2 photocatalysts with engineered facets for enhanced degradation of bisphenol A through persulfate activation. *Appl. Catal. B-Environ.* 268, 118394.
- Tanwar, R., Kumar, S., Mandal, U.K., 2017. Photocatalytic activity of PANI/ Fe^0 doped BiOCl under visible light-degradation of Congo red dye. *J. Photoch. Photobio. A* 333, 105–116.
- Wang, C.-W., Liang, C., 2014. Oxidative degradation of TMAH solution with UV persulfate activation. *Chem. Eng. J.* 254, 472–478.
- Wang, N., Zhu, L., Deng, K., She, Y., Yu, Y., Tang, H., 2010. Visible light photocatalytic reduction of Cr(VI) on TiO_2 in situ modified with small molecular weight organic acids. *Appl. Catal. B-Environ.* 95, 400–407.
- Wang, C.-C., Li, J.-R., Lv, X.-L., Zhang, Y.-Q., Guo, G., 2014. Photocatalytic organic pollutants degradation in metal-organic frameworks. *Energy Environ. Sci.* 7, 2831–2867.
- Wang, C.-C., Du, X.-D., Li, J., Guo, X.-X., Wang, P., Zhang, J., 2016. Photocatalytic Cr(VI) reduction in metal-organic frameworks: a mini-review. *Appl. Catal. B-Environ.* 193, 198–216.
- Wang, C.-Y., Zhang, X., Qiu, H.-B., Wang, W.-K., Huang, G.-X., Jiang, J., Yu, H.-Q., 2017a. Photocatalytic degradation of bisphenol A by oxygen-rich and highly visible-light responsive $\text{Bi}_{12}\text{O}_{17}\text{Cl}_2$ nanobelts. *Appl. Catal. B-Environ.* 200, 659–665.
- Wang, Y., Zhao, X., Cao, D., Wang, Y., Zhu, Y., 2017b. Peroxymonosulfate enhanced visible light photocatalytic degradation bisphenol A by single-atom dispersed Ag mesoporous g- C_3N_4 hybrid. *Appl. Catal. B-Environ.* 211, 79–88.
- Wang, C., Xue, Y., Wang, P., Ao, Y., 2018. Effects of water environmental factors on the photocatalytic degradation of sulfamethoxazole by Ag/ $\text{UiO}-66$ composite under visible light irradiation. *J. Alloy. Compd.* 748, 314–322.
- Wang, C., Kim, J., Malgras, V., Na, J., Lin, J., You, J., Zhang, M., Li, J., Yamauchi, Y., 2019a. Metal-organic frameworks and their derived materials: emerging catalysts for a sulfate radicals-based advanced oxidation process in water purification. *Small* 15, 1900744.
- Wang, S., Wu, J., Lu, X., Xu, W., Gong, Q., Ding, J., Dan, B., Xie, P., 2019b. Removal of acetaminophen in the Fe^{2+} /persulfate system: kinetic model and degradation pathways. *Chem. Eng. J.* 358, 1091–1100.
- Wang, Z., Huang, J., Mao, J., Guo, Q., Chen, Z., Lai, Y., 2020. Metal-organic frameworks and their derivatives with graphene composites: preparation and applications in electrocatalysis and photocatalysis. *J. Mater. Chem. A* 8, 2934–2961.
- Wei, J., Liu, Y., Zhu, Y., Li, J., 2020. Enhanced catalytic degradation of tetracycline antibiotic by persulfate activated with modified sludge bio-hydrochar. *Chemosphere* 247, 125854.
- Wright-Walters, M., Volz, C., Talbot, E., Davis, D., 2011. An updated weight of evidence approach to the aquatic hazard assessment of Bisphenol A and the derivation of a new predicted no effect concentration (PNEC) using a non-parametric methodology. *Sci. Total Environ.* 409, 676–685.
- Xu, B., Chen, Z., Han, B., Li, C., 2017. Glycol assisted synthesis of MIL-100(Fe) nanospheres for photocatalytic oxidation of benzene to phenol. *Catal. Commun.* 98, 112–115.
- Xu, Y., Ma, Y., Ji, X., Huang, S., Xia, J., Xie, M., Yan, J., Xu, H., Li, H., 2019. Conjugated conducting polymers PANI decorated $\text{Bi}_{12}\text{O}_{17}\text{Cl}_2$ photocatalyst with extended light response range and enhanced photoactivity. *Appl. Surf. Sci.* 464, 552–561.
- Yang, Y., Wang, G., Deng, Q., Ng, D.H.L., Zhao, H., 2014. Microwave-assisted fabrication of nanoparticulate TiO_2 microspheres for synergistic photocatalytic removal of Cr(VI) and methyl orange. *ACS Appl. Mater. Inter.* 6, 3008–3015.
- Yang, Z.-Z., Zhang, C., Zeng, G.-M., Tan, X.-F., Wang, H., Huang, D.-L., Yang, K.-H., Wei, J.-J., Ma, C., Nie, K., 2020. Design and engineering of layered double hydroxide based

- catalysts for water depollution by advanced oxidation processes: a review. *J. Mater. Chem. A* 8, 4141–4173.
- Yi, X.-H., Ma, S.-Q., Du, X.-D., Zhao, C., Fu, H., Wang, P., Wang, C.-C., 2019. The facile fabrication of 2D/3D Z-scheme g-C₃N₄/UiO-66 heterojunction with enhanced photocatalytic Cr(VI) reduction performance under white light. *Chem. Eng. J.* 375, 121944.
- Yu, J., Ran, J., 2011. Facile preparation and enhanced photocatalytic H₂-production activity of Cu(OH)₂ cluster modified TiO₂. *Energy Environ. Sci.* 4, 1364–1371.
- Yuan, R., Zhu, Y., Zhou, B., Hu, J., 2019. Photocatalytic oxidation of sulfamethoxazole in the presence of TiO₂: effect of matrix in aqueous solution on decomposition mechanisms. *Chem. Eng. J.* 359, 1527–1536.
- Zeng, T., Zhang, X., Wang, S., Niu, H., Cai, Y., 2015. Spatial confinement of a Co₃O₄ catalyst in hollow metal–organic frameworks as a nanoreactor for improved degradation of organic pollutants. *Environ. Sci. Technol.* 49, 2350–2357.
- Zhang, C., Ai, L., Jiang, J., 2015a. Solvothermal synthesis of MIL-53(Fe) hybrid magnetic composites for photoelectrochemical water oxidation and organic pollutant photodegradation under visible light. *J. Mater. Chem. A* 3, 3074–3081.
- Zhang, F., Shi, J., Jin, Y., Fu, Y., Zhong, Y., Zhu, W., 2015b. Facile synthesis of MIL-100(Fe) under HF-free conditions and its application in the acetalization of aldehydes with diols. *Chem. Eng. J.* 259, 183–190.
- Zhao, J., Han, Q., Zhu, J., Wu, X., Wang, X., 2014. Synthesis of Bi nanowire networks and their superior photocatalytic activity for Cr(VI) reduction. *Nanoscale* 6, 10062–10070.
- Zhao, C., Wang, Z., Wang, C., Li, X., Wang, C.-C., 2018a. Photocatalytic degradation of DOM in urban stormwater runoff with TiO₂ nanoparticles under UV light irradiation: EEM-PARAFAC analysis and influence of co-existing inorganic ions. *Environ. Pollut.* 243, 177–188.
- Zhao, X., Du, P., Cai, Z., Wang, T., Fu, J., Liu, W., 2018b. Photocatalysis of bisphenol A by an easy-settling titania/titanate composite: effects of water chemistry factors, degradation pathway and theoretical calculation. *Environ. Pollut.* 232, 580–590.
- Zhao, C., Wang, Z., Li, X., Yi, X., Chu, H., Chen, X., Wang, C.-C., 2020. Facile fabrication of BUC-21/Bi₂₄O₃₁Br₁₀ composites for enhanced photocatalytic Cr(VI) reduction under white light. *Chem. Eng. J.* 389, 123431.
- Zheng, J., Jiao, Z., 2017. Modified Bi₂WO₆ with metal-organic frameworks for enhanced photocatalytic activity under visible light. *J. Colloid Interf. Sci.* 488, 234–239.
- Zheng, J., Chang, F., Jiao, M., Xu, Q., Deng, B., Hu, X., 2018. A visible-light-driven heterojunction composite WO₃/Bi₁₂O₁₇Cl₂: synthesis, characterization, and improved photocatalytic performance. *J. Colloid Interf. Sci.* 510, 20–31.
- Zhou, C., Lai, C., Xu, P., Zeng, G., Huang, D., Zhang, C., Cheng, M., Hu, L., Wan, J., Liu, Y., Xiong, W., Deng, Y., Wen, M., 2018. In situ grown AgI/Bi₁₂O₁₇Cl₂ heterojunction photocatalysts for visible light degradation of sulfamethazine: efficiency, pathway, and mechanism. *ACS Sustain. Chem. Eng.* 6, 4174–4184.